DOI: https://doi.org/10.2138/am-2022-8080. http://www.minsocam.org/

Revision 2

Hydrothermal monazite trumps rutile: applying U-Pb geochronology to evaluate complex mineralization ages of the Katbasu Au-Cu deposit, Western Tianshan, Northwest China

Jiahao Zheng[1,2*], Ping Shen[2], Wanyi Feng[3]

[1] Department of Earth and Space Sciences, Southern University of Science and Technology, Shenzhen 518055, China

[2] Key Laboratory of Mineral Resources, Institute of Geology and Geophysics, Chinese Academy of Sciences, Beijing 100029, China

[3] Department of Ocean Science and Engineering, Southern University of Science and Technology, Shenzhen 518055, China

*Corresponding author: Dr. Jiahao Zheng

Email address: joey-zen@163.com

Southern University of Science and Technology, 1088 Xueyuan Avenue, Shenzhen 518055, China

Phone: +86 0755-88018862; fax: +86 0755-88015519.

Abstract

The Tianshan orogenic belt hosts several world-class gold deposits and is one of the largest gold provinces on Earth. The Katbasu Au-Cu deposit in the Chinese Western Tianshan is hosted in a granite intrusion. Previous researchers have shown that the main gold ores formed much later than the ore-hosting granite. However, the formation age of Cu mineralization and its possible link to Au mineralization remain poorly understood. This paper reports detailed mineralogical studies, combined with zircon U-Pb, in situ hydrothermal monazite as well as rutile U-Pb ages to constrain the timing of Cu mineralization and its possible link to Au mineralization. The two main ore types in the Katbasu deposit include Cu-Au ores with pyrite-chalcopyrite veins, which crosscut the granite, and Au ores with massive pyrite and quartz as the main minerals. The Cu-Au ores are spatially associated with diorite that intruded the granite, and they are overprinted by massive gold ores. Detailed mineralogical studies show that chalcopyrite is the main Cu-bearing mineral in the Cu-Au ores, and it is closely associated with some native gold, monazite, and rutile.

Secondary ion mass spectrometer (SIMS) U-Pb dating of zircon grains from the ore-hosting granite and mafic enclave yielded concordant ages of 354.1 ± 1.6 Ma and 355.8 ± 1.7 Ma, respectively. The diorite that intruded the granite has a zircon U-Pb age of 352.0 ± 3.2 Ma. The trace element compositions of the monazite suggest they were formed by hydrothermal fluids rather than inherited from the ore-hosting granite. Hydrothermal monazite coexisting with chalcopyrite and native gold yielded a concordant age of 348.7 ± 2.3 Ma, and the W-rich hydrothermal rutile grains associated with the chalcopyrite yielded a U-Pb age of 345 ± 27 Ma, indicating an early Cu-Au mineralization event prior to the major Au mineralization (ca. 323-311 Ma). The formation time of early Cu-Au mineralization is consistent with the emplacement age of the diorite and may be of magmatic-hydrothermal origin, whereas the main Au has no genetic associations with magmatic rocks in the ore district and may belong to the orogenic type. Monazite geochronology provided a more reliable age constraint than rutile in the Katbasu Au-Cu deposit, and we suggest hydrothermal monazite has advantages over rutile in dating the mineralization ages of gold deposits.

***Keywords*:** Hydrothermal monazite; Rutile; Geochronology; Katbasu Au-Cu deposit; Western Tianshan

1. Introduction

The formation ages of ore deposits are critical for understanding their genesis and making exploration strategies. Among various types of ore deposit, it is notoriously difficult to determine the age of gold deposits due to a lack of suitable dating minerals (e.g., Stein 2014; Zheng et al. 2020). The most commonly used dating methods in gold deposits include sericite $^{40}Ar/^{39}Ar$ ages (Goldfarb et al. 1991; Mao et al. 2004; Li et al. 2012), arsenopyrite and pyrite Re-Os ages (Kirk et al. 2002; Morelli et al. 2007; Le Mignot et al. 2017), and to a lesser extent molybdenite Re-Os ages

DOI: https://doi.org/10.2138/am-2022-8080. http://www.minsocam.org/

(Selby et al. 2002; Zhai et al. 2019). Dating the gold mineralization ages using the abovementioned methods can be challenging due to (1) sericite with low closure temperatures may yield mixed ages induced by multiple hydrothermal events (Chiaradia et al. 2013), (2) extremely low Re and Os contents in many arsenopyrite and pyrite grains make it difficult to produce a reliable isochron age (Stein et al. 2000), and (3) molybdenite is rare in most gold deposits. In addition to pyrite, arsenopyrite, and sericite, hydrothermal monazite and rutile have been observed in many gold deposits, and their U-Th-Pb ages have also been used to constrain the timing of gold mineralization (Jemielita et al. 1990; Rasmussen et al. 2006; Cabral et al. 2013; Fielding et al., 2017; Deng et al. 2020). However, there has been little attempt to evaluate the relative accuracy and suitability between hydrothermal monazite and rutile in gold deposits.

Located in the southern part of the Central Asian Orogenic Belt (CAOB), the Tianshan belt (also known as Tien Shan) stretches for more than 2000 km across Uzbekistan and Kyrgyzstan to Xinjiang in China. It hosts several world-class gold deposits (e.g., Muruntau with 6137 t Au, Frimmel 2008; Almalyk with 2000 t Au, Cooke et al. 2005; and Kumtor with 1100 t Au, Mao et al. 2004), and is one of the largest Phanerozoic gold provinces on Earth. The Chinese Western Tianshan orogenic belt in Xinjiang hosts many Paleozoic gold deposits and occurrences, several of which contain ore reserves more than 50 tons (e.g., Sawayaerdun orogenic gold deposit with 130 t Au, Liu et al. 2002; Axi and Jingxi-Yelmand epithermal gold deposits with 70 t and 95 t Au, White 2007), and it is one of the most important gold ore belts in China

(Zhu et al. 2016). Previous researchers have documented the geological characteristics, nature of the ore fluids, ore-forming ages, stable and radioactive isotopes, as well as geodynamic settings of these gold deposits (e.g., Long et al. 2005; Chiaradia et al. 2006; Liu et al. 2007; Zhai et al. 2009; Zhu 2011; Chen et al. 2012; Zheng et al. 2016; An and Zhu 2018).

The Katbasu deposit is a newly discovered Au-Cu deposit in the Chinese Western Tianshan with a gold reserve of 87 t at an average grade of 3.84 g/t, and copper reserves of 50,000 tons (Yang et al. 2013; Xing et al. 2018). Since 2008, regional geological field mapping and chemical sampling at Katbasu led to the identification of an alteration and mineralization zone. Subsequent geological and geophysical surveys, followed by drilling programs during 2011 to 2012, confirmed the discovery of a large Au-Cu deposit hosted in the granite (Yang et al. 2013). Recent researchers have elaborated on the chronology and genesis of ore-hosting granites, ore deposit geology, structural characteristics, gold mineralization ages, fluid inclusions, and H-O-S-Pb isotopes of the Katbasu gold-copper deposit (Feng et al. 2014; Gao et al. 2015; Zhang et al. 2015; Dong et al. 2018; Liu et al. 2018; Zhao et al. 2019). The diachronous ages of pyrite in the Katbasu deposit (310.9 $\pm$ 4.2 Ma from pyrite Re-Os, Zhang et al. 2015; 322.5 $\pm$ 6.8 Ma from pyrite Rb-Sr, Dong et al. 2018) indicate that the gold mineralization occurred much later than the ore-hosting granite (zircon U-Pb ages of 359.8 -345.5 Ma, Feng et al. 2014; Dong et al. 2018; Li et al. 2018). However, the timing of copper mineralization and its potential links with gold mineralization in the Katbasu deposit is not clear, and its genesis remains

DOI: https://doi.org/10.2138/am-2022-8080. http://www.minsocam.org/

controversial. Our recent study on the Katbasu Au-Cu deposit found that in addition to a large amount of pyrite and quartz, the Au-Cu ores also contain many hydrothermal monazite and rutile grains. Detailed mineralogical studies have shown that these hydrothermal monazite and rutile grains are closely related to chalcopyrite and native gold. These findings make the Katbasu deposit an ideal object for studying the relative accuracy and suitability of monazite and rutile chronology in hydrothermal gold deposits.

In this contribution, we use geological observation and detailed mineralogy, together with zircon, hydrothermal monazite, and rutile chronology in the Katbasu Au-Cu deposit, with aims to (1) study the Cu mineralization age of the Katbasu gold deposit and its potential links to the Au mineralization; (2) discuss the genetic type of the Katbasu deposit; and (3) evaluate the relative accuracy and suitability between hydrothermal monazite and rutile for geochronology in gold deposits.

2. Regional geology

The Chinese Western Tianshan, situated in the southern part of the Central Asian Orogenic Belt (CAOB; Fig. 1a), is herein defined as all parts of the mountain range in China located west of the Urumqi-Korla Road, and bounded by the southern margin of the Junggar Basin and the northern margin of Tarim Basin (Fig. 1b). It was formed by the amalgamations of the Tarim, Yili, and Junggar blocks (Gao et al. 1998; Zhu et al. 2009). It can be further divided into the North Tianshan Accretionary Complex (NTAC), the Yili-Central Tianshan, and the South Tianshan Orogenic Belt (STOB)

DOI: https://doi.org/10.2138/am-2022-8080. http://www.minsocam.org/

from north to south.

The NTAC is mainly composed of Devonian to Early Carboniferous volcanic and sedimentary rocks, and ophiolitic slices (Feng and Zhu 2018). It was formed by southward subduction of North Tianshan ocean beneath Yili-Central Tianshan along the North Tianshan suture zone. The Yili-Central Tianshan contains a Precambrian basement and overlying Paleozoic volcanic-sedimentary strata. Voluminous granitoid plutons intruded into the Ordovician-Early Carboniferous volcanic-sedimentary strata (Feng and Zhu 2019). The STOB mainly consists of Lower Cambrian-Carboniferous sedimentary rocks and interlayered volcanic rocks, high/ultrahigh pressure metamorphic rocks, ophiolitic components, and Permian granitoids (Gao et al. 2009).

The Katbasu Au deposit is located in the southern part of the Yili-Central Tianshan terrane, adjacent to the northern part of the STOB (Fig. 1b). The South Tianshan oceanic slab subducted northwards beneath the Yili-Central Tianshan in the Early Silurian, producing the continental arc magmatism. The subduction probably terminated in the Late Carboniferous, and subsequent orogenesis occurred between Late Carboniferous and Early Permian (Feng and Zhu 2019). The NEE trending North Nalati fault and the South Nalati fault are the two major regional faults in this area, and some E-W and NEE striking faults occur as secondary structures (Fig. 2a). The strata that crop out north of the North Nalati fault are mainly Carboniferous volcanic-sedimentary rocks. The main intrusive rocks in the region are Carboniferous granitoids, as well as some Silurian, Devonian, and Permian granitoids.

3. Deposit geology and mineralization

The Katbasu deposit contains gold reserve of about 87 t and copper reserves of 50,000 tons (Xing et al., 2018). In the Katbasu mining area, the volcano-sedimentary succession is mainly composed of Silurian tuff and limestone (Fig. 2b). Some unmineralized garnet-epidote skarn occurs locally at the boundary between granitoids and limestone. Several NEE-trending faults in the mining area, and the main gold orebodies are located in the granite between F5 and F6 faults. The igneous rocks in the Katbasu Au deposit consist mainly of granite, granodiorite, and diorite (Figs. 2b and c). The granite is a homogeneous pluton emplaced in a single phase. Some mafic enclaves occur in the granite, and they have diffuse contacts with the hosting granite (Fig. 3b). The mafic enclaves typically have rounded shapes, but may be subangular. The mafic enclaves have relatively homogenous mineral sizes and textures from their rims to cores, indicating that they crystallized almost coevally with the hosting granite. The granite (Fig. 3a) consists of potassium feldspar, plagioclase, quartz, and minor biotite, whereas the mafic enclaves are composed mainly of plagioclase and biotite. Some diorite dikes intruded the granite pluton, and they generally have sharp contacts with the hosting granite as some Cu-Au mineralization occurs at their contact zones (Xing et al. 2016). The diorites are composed mainly of plagioclase and amphibole with some disseminated pyrite and chalcopyrite (Figs. 3c and 4a).

The orebodies are spatially associated with the Early Carboniferous granite. The main Au orebodies are distributed between the F5 and F6 faults and nearly parallel to them. Ore-hosting granite in the Katbasu deposit include various types of potassic, chlorite, and sulfide-quartz vein alterations. Orebodies of the Katbasu Au deposit are usually lens-shaped and hosted in the granite (Figs. 2b and c). The ore-hosting granite has been dated between 359 and 346 Ma by LA-ICP MS and SIMS zircon U-Pb methods (Feng et al. 2014; Zhang et al. 2015; Dong et al. 2018). The Katbasu deposit mainly consists of two types of ores: (1) the vein type Cu-Au ores with pyrite -chalcopyrite veins/veinlets crosscutting or enclosed in the granite (Fig. 3e), and (2) massive Au ores mainly occur as veins that generally have a sharp contact with the host granite or locally replace the granite, and pyrite and quartz as main minerals (Figs. 3g and h). Massive gold ore is the main ore type of the Katbasu deposit, accounting for more than 90% of the total ores. By contrast, the Cu-Au ores are relatively small in scale, and mainly occur in the footwall. The two types of ores are generally spatially separated, though locally small parts of Cu-Au ores are overprinted by massive gold ores. Some Cu-Au mineralization occurred in the contact area where the diorite dikes intruded into the granite pluton (Xing et al. 2016). The massive Au ores mainly occur as tabular or lenses dipping to the south, with the dip angles varying between ~20° and 70°. The Cu-Au ores and massive Au ores are nearly parallel. The thickness of the vein type Cu-Au orebody mainly ranges between several centimeters and tens of centimeters, whereas the thickness of the massive Au orebody varies mainly from tens of centimeters to several meters.

Pyrite is the predominant ore mineral in the Katbasu Au deposit, and it precipitated in all ore-forming processes (Figs. 4 and 5). Other ore minerals include chalcopyrite, native gold, scheelite, and Te-Bi minerals. The gangue minerals consist of sericite, quartz, rutile, monazite, apatite, and calcite. Gold mainly occurs as native gold in the massive Au and veinlet Cu-Au ores. Minor petzite was found in the veinlet Cu-Au ores. Native gold usually occurs in pyrite and chalcopyrite as inclusions or fills fractures in pyrites, with small amounts of native gold found in the quartz. Native gold grains mainly vary between ~ 3 μm and 40 μm in size. There is no obvious difference in the size or fineness of the native gold between the two types of ores. The mineralogy and compositions of the Te-Bi minerals (Fig. 5) have been studied in detail using the scanning electron microscopy (SEM). The Te-Bi minerals, consisting mostly of tetradymite (Bi_2Te_2S), hessite (Ag_2Te), and petzite (Ag_3AuTe_2), are hosted irregularly in pyrite and chalcopyrite fractures and voids.

On the basis of the paragenesis, four stages of sulfides are recognized (Fig. 6). Disseminated pyrite (Py1) grains occurring in the granite and are the products of early hydrothermal alterations (Figs. 3d and 4d). Py1 occurs as anhedral crystals with a porous texture filled by quartz and has no genetic associations to gold or copper minerals, which formed prior to mineralization and are attributed to the pre-ore stage (Stage 1). The subsequent Cu-Au mineralization stage (Stage 2) occurred as veins or veinlets that crosscut the granite, and mainly consists of pyrite (Py2), chalcopyrite, native gold, rutile, and monazite (Figs .3e, 4e, g, and h), as well as some tetradymite, hessite, and petzite (Figs. 5a-d). Py2 occurs as medium- to coarse-grained, anhedral crystal aggregates that coexists with chalcopyrite and native gold. Monazite is intergrown with the native gold-hosting chalcopyrite crystals. Rutile coexists with chalcopyrite and pyrite grains. Two distinct types of rutile, namely early rutile (Rt1)

DOI: https://doi.org/10.2138/am-2022-8080. http://www.minsocam.org/

and late rutile (Rt2), have been recognized. The main Au ore stage (Stage 3) minerals are dominated by pyrite (Py3) and quartz, some native gold, as well as minor rutile, scheelite, and apatite (Figs. 4i and 5e). Py3 occurs as coarse-grained, anhedral crystal aggregates with porous textures filled by quartz and some native gold. The post-ore calcite veins formed away from ores, and are mainly composed of calcite and fine-grained pyrite (Py4). Py4 occurs as isolated, and subhedral to euhedral grains with no obvious porous texture (Figs. 3i and 5f).

4. Analytical techniques

4.1. Zircon U-Pb dating

Zircon grains from the ore-hosting granite (sample KT17-187; Fig. 3a), mafic enclave (sample KT17-197; Fig. 3b), and diorite (sample KT17-9; Fig. 3c) were separated using a conventional magnetic and density technique and hand-picked under a binocular microscope. The selected zircon grains were mounted in epoxy resin. Prior to analyses, all the selected zircon grains were examined with reflected and transmitted light photomicrographs combined with cathodoluminescence (CL) images (Figs. 7 and 8a) to reveal their internal structures. Zircons with a few inclusions or fissures were chosen for U-Pb dating during this study.

Zircon U-Pb analyses of ore-hosting granite and mafic enclave were performed using the Cameca IMS 1280 ion microprobe at the Guangzhou Institute of Geochemistry, Chinese Academy of Sciences (GIGCAS). The ellipsoidal spot for zircon U-Pb dating is about 30× 20 μm in size. Detailed operating and data processing

DOI: https://doi.org/10.2138/am-2022-8080. http://www.minsocam.org/

procedures are similar to those described by Li et al. (2009). Measured Pb/U ratios were calibrated relative to the zircon standard Plešovice (Sláma et al. 2008). Non-radiogenic Pb was subtracted from the measured Pb isotopic composition using the measured ^{204}Pb and the present-day average terrestrial Pb isotopic composition in the model of Stacey and Kramers (1975). Uncertainties on individual analyses in data tables are reported at a 1σ level. Mean ages for pooled U/Pb (and Pb/Pb) analyses are quoted with 95% confidence interval. Data reduction was carried out using the Isoplot 3.00 program (Ludwig 2003).

The U-Pb isotopic analyses of the diorite were carried out by a GeolasPro laser ablation system coupled with a multi-collector inductively coupled plasma mass spectrometer (MC-ICP MS) at the Sample Solution Analytical Technology Co., Ltd. (SSATC) in the Hubei province, Wuhan, China. The analytical spot size was about 32 μm in diameter. An Agilent 7700e ICP-MS instrument was used to acquire ion-signal intensities, and He was applied as a carrier gas. Zircon sample 91500 was used as the external standard, and zircon standards GJ-1 and Plešovice were used as unknown samples to monitor the stability and accuracy of the acquired U-Pb data. The data selection and calibration were performed by the ICPMSDataCal (Liu et al. 2010). Correction for common Pb was applied using the method described by Andersen (2002). Weighted mean calculations and concordia diagrams were made using the Isoplot 3.00 program (Ludwig 2003).

4.2 Monazite U-Pb isotopic analyses

The monazite-bearing auriferous sample was collected from the veinlet ores (Figs. 3e and 4g). LA-ICP-MS data collection for both ages and trace element abundance was performed simultaneously at the SSATC. Laser sampling was performed using a GeolasPro laser ablation system that consists of a COMPexPro 102 ArF excimer laser. An Agilent 7700e ICP-MS instrument was used to acquire ion-signal intensities. Helium was applied as a carrier gas. Argon was used as the make-up gas and mixed with the carrier gas via a T-connector before entering the ICP. The spot size and frequency of the laser were set to 16 μm and 2 Hz, respectively. Monazite standard TRE and 44069 and glass NIST610 were used as external standards for U-Pb dating and trace element calibration, respectively. Each analysis incorporated a background acquisition of approximately 20-30 s followed by 50 s of data acquisition from the sample. An Excel-based software ICPMSDataCal was used to perform off-line selection and integration of background and analyzed signals, time-drift correction, and quantitative calibration for trace element analysis and U-Pb dating (Liu et al. 2010). Concordia diagrams and weighted mean calculations were made using the Isoplot 3.00 program (Ludwig 2003).

4.3. In situ rutile Raman spectroscopy, Electron microprobe analysis, and SIMS U-Pb dating

Although trace elements can be used to discriminate between rutile, anatase, and brookite (Triebold et al. 2011; Plavsa et al. 2018), the most reliable method to distinguish between the three mineral polymorphs is laser Raman spectroscopy

(Meinhold 2010). Thus, before U-Pb isotope analysis, Raman spectroscopy was conducted on the rutile sample at 100 - 4000 cm^{-1} using a LabRam HR800 laser Raman microspectrometer at the IGGCAS. The incident radiation was provided by an argon ion laser with a wavelength of 532 nm and a source power of 44 mW.

Major and minor element compositions of the selected rutile grains were determined using a JEOL JXA-8230 electron probe under operating conditions of 15 kV, a 2 μm 10 nA beam, a count time of 10 s (peak) and 5 s for the upper and lower background, at the Fuzhou University, Fuzhou, China. Natural and synthetic minerals were used for standard calibration. The ZAF correction method was used to correct the atomic number (Z), absorption (A), and fluorescence (F) effects for all analyzed minerals.

Rutile crystals, coexisting with chalcopyrite (Figs. 4b and c), were drilled from the thin section and then mounted in a transparent epoxy together with the DXK rutile standard ($^{206}Pb/^{238}U$ age = 1782.6 ± 2.8 Ma, Li et al. 2013) and an in-house rutile standard JDX ($^{206}Pb/^{238}U$ age = 509 ± 8 Ma, Li et al. 2011). The *in-situ* of U - Pb isotope measurements of rutile were performed using a CAMECA IMS-1280 ion microprobe at IGGCAS. The instrumental conditions and measurement procedures were similar to those described by Li et al. (2011). The ellipsoidal spot was about 30 × 20 μm in size. Each measurement comprises 10 cycles during a total analytical duration of ~ 15 minutes, including 2 minutes rastering prior to the actual analysis to reduce the contribution of surface Pb contaminants. The DXK rutile was used as the standard to calibrate the Pb/U fractionation, and JDX rutile as an unknown to monitor the whole analytical procedure. The U-Pb isotopic ages were calculated using the decay constants recommended by Sterger and Jäger (1977) and the Isoplot 3.00 program (Ludwig 2003).

5. Results

5.1 Zircon U-Pb ages

Zircon U-Pb dating results of the ore-hosting granite and the mafic enclaves are listed in Table 1. The CL images of representative zircon grains from the ore-hosting granite and mafic enclave are shown in the Figure 7. Based on photomicrographs and CL images, analytical sites with few inclusions or fissures were chosen for U-Pb dating during this study. Most zircon grains from the ore-hosting granite exhibit oscillatory zoning with no obvious rim to core textural differences. They have a prolate axis length of ~80-250 μm, with length/width ratios between 1:1 and 2:1. They yielded high Th/U ratios of 0.57 to 1.10, consistent with a magmatic origin. All ten spot analyses yielded a concordia age of 354.1 ± 1.6 Ma (MSWD=1.8) (Fig. 7a). This age is interpreted as the crystallization age of the ore-hosting granite. Zircon grains from the mafic enclave have darker CL images than those from the granite. They generally show a dark core overgrown by a thin bright rim (Fig. 7b). They have a length of ~60 to 150 μm, with length/width ratios between 1:1 and 1.5:1. Because the rim is too thin to be analyzed, only the cores were analyzed. They have high Th/U ratios of 0.92 to 3.23. Eight spot analyses gave a concordia age of 355.8 ± 1.7

Ma (MSWD = 0.68) (Fig. 7b), which is interpreted as the crystallization age of the mafic enclave.

Zircon U-Pb dating results of diorite are listed in Table 2. Similar to the mafic enclaves, zircon grains in the diorite generally have a dark core and a thin bright rim. They have a length of ~50-130 μm, with length/width ratios between 1:1 and 2:1. They have Th/U ratios ranging from 0.05 to 1.08. All 18 spot analyses yielded a wide range of $^{206}Pb/^{238}U$ ages varying from 349.4 ± 3.2 Ma to 401.2 ± 4.7 Ma. Given the geological fact that the diorite intruded in the granite, the $^{206}Pb/^{238}U$ ages older than 360 Ma may indicate a mixing in of xenocrystic zircons from the strata during ascent of the magma rather than the crystallization age of the diorite. Fourteen spots with ^{206}Pb-^{238}U ages older than 360 Ma, varying from 361.9 Ma to 401.2 Ma, define a weighted mean age of 373.7 ± 5.9 Ma (MSWD = 6.3; Fig. 8b). Four spot analyses younger than 360 Ma (Fig. 8c) gave a weighted mean age of 352.0 ± 3.2 Ma (MSWD = 0.52; Fig. 8d), which is interpreted as the crystallization age of the diorite.

5.2 Monazite U-Pb age and trace elements

LA-ICP-MS U-Pb dating results are given in Table 3. Monazite is closely associated with gold-hosting chalcopyrite, and the BSE images show that monazite is compositionally homogeneous without observable zoning (Figs. 4g and h). No magmatic monazite was found within the host granite or diorite. Monazite in the ores occurs as elongated or irregular grains from less than 10 to ~100 μm in size. The monazite contains relatively low amounts of Th (494-2790 ppm) and U (308-1494 ppm), yielding Th/U ratios of 0.4 to 9.1. These relatively low Th and U content are much lower than the magmatic monazite, but consistent with the compositions of hydrothermal monazite (Fig. 9a; Schandl and Gorton 2004; Taylor et al. 2015). Twenty-seven monazite analyses yielded a concordant $^{206}Pb/^{238}U$ age of 348.6 ± 0.9 Ma (1σ, MSWD = 3.1; Fig. 9c), with a weighted mean age of 348.7 ± 2.3 Ma (2σ, MSWD = 1.6; Fig. 9d).

The trace element results for monazite are listed in Supplemental Table 1. The monazite samples display relatively coherent LREE enriched and HREE depleted patterns with obvious negative Eu anomalies.

5.3 In situ rutile Raman analyses, trace elements, and U-Pb age

Two types of TiO_2 minerals in the Katbasu ores are characterized by the peaks at wavenumbers 142, 228, 445, and 612 cm^{-1} for Rt1, and 142, 228, 445, and 610 cm^{-1} for Rt2, respectively (Fig. 10c). These spectra are similar with those from rutile, but inconsistent with those from brookite and anatase (Fig. 10d; Meinhold 2010), suggesting the TiO_2 minerals in the Katbasu ores are rutile.

The EMPA results for two types of rutile are listed in Supplemental Table 2. The early formed rutile (Rt1) has relatively low TiO_2 content (85.27-90.31 wt.%) but a high WO_3 content varying between 3.57 and 7.09 wt.%. By contrast, the late formed rutile (Rt2) has nearly pure TiO_2 endmember compositions (94.31-99.78 wt.%) with a low WO_3 content ranging from 0.01 to 0.33 wt.%. In addition to TiO_2 and WO_3, Rt1 also contains higher Nb and Fe contents (0.91-5.21 wt.% and 0.36-1.92 wt.%) than those from Rt2 (0.15-1.67 wt.% and 0.04-0.46 wt.%).

A total of sixteen measurements were conducted on the selected W-rich Rt1 crystals from the Katbasu gold deposit. The U-Pb isotopic data for the analyzed rutile grains are listed in Table 4 and illustrated in Figure 11. The measured U contents vary from 6 to 172 ppm. Regression of the data points on the Tera-Wasserburg plot gives a lower intercept age of 345 ± 27 Ma (MSWD = 3.3). The discordance age of rutile may be caused by mixtures of heterochemical, resolvably diachronous rutile generations in petrologic disequilibrium (Fig. 10; Villa and Hanchar, 2017).

6. Discussion

6.1 Age constraints on magmatism and mineralization in the Katbasu Au-Cu deposit

Previous zircon U-Pb dating results of magmatic rocks in the Katbasu ore district include ore-hosting granite, granodiorite, and rhyolite, which yielded ages of 359.8 ± 5.2 Ma to 345.5 ± 2.6 Ma, 355.7 ± 2.7 Ma, and 335.7 ± 1.1 Ma (Feng et al. 2014; Zhang et al. 2015; Dong et al. 2018; Li et al. 2018), respectively. In particular, the zircon U-Pb ages of the ore-hosting granite vary widely from 359.8 ± 5.2 Ma to 345.5 ± 2.6 Ma. It is therefore necessary to evaluate the reliability of our age. The geological relations among the granite, mafic enclave, and diorite dike indicates that the mafic enclave and diorite dike were formed before and after the granite, respectively. The zircon U-Pb ages of the mafic enclaves, ore-hosting granite, and diorite obtained in this study are 355.8 ± 1.7 Ma, 354.1 ± 1.6 Ma, and 352.0 ± 3.2 Ma, respectively. This is consistent with the geological facts, indicating that the ore-hosting granite formed at ca. 354 Ma.

Gold in Katbasu Au-Cu deposit is mainly hosted in the massive quartz-sulfide ores. Rb-Sr and Re-Os isochron ages of the auriferous pyrite are 322.5 ± 6.8 Ma (Dong et al. 2018) and 310.9 ± 4.2 Ma (Zhang et al. 2015), respectively. These geochronological results show that the formation time of the main gold mineralization is obviously later than that of the ore-hosting granite. However, the formation time of copper mineralization and its possible links to gold mineralization remains poorly understood. The paragenesis of the minerals indicates that chalcopyrite is closely related to native gold, monazite, and rutile in the stockwork ore (Figs. 4e,f,g, and h), indicating a Cu-Au mineralization independent of the main Au mineralization. Thus, if the monazite and rutile were formed by hydrothermal fluids instead of having been inherited from the wall rock granite, the ages of monazite and rutile would represent the timing of Cu-Au mineralization in the Katbasu deposit.

Previous studies have shown that magmatic and hydrothermal monazite can be effectively distinguished by their trace elements (Taylor et al. 2015; Zi et al. 2015; Piechocka et al. 2017). The monazite associated with Cu-Au mineralization have relatively low Th and U contents as well as Th/U ratios (Fig. 9a and b), which are consistent with the compositions of hydrothermal monazite but different from those with magmatic origins (Taylor et al. 2015; Piechocka et al. 2017). In addition, no magmatic monazite was found in the Katbasu ore-hosting granite, indicating that the monazite was not inherited from the granite. Thus, we consider that the monazite grains originated from hydrothermal fluids rather than inherited from the ore-hosting granite. To date, there is no effective criteria to distinguish between rutile with a magmatic or hydrothermal origin (Meinhold 2010). The rutile grains associated with the sulfides are W-rich. Tungsten-rich rutile grains have been found in many hydrothermal gold deposits (Dostal et al. 2009; Scott et al. 2011; Agangi et al. 2019). Therefore, we consider that the ages of the monazite and W-rich hydrothermal rutile record the time of Au-Cu mineralization in the Katbasu deposit.

The hydrothermal monazite U-Pb age is 348.7 ± 2.3 Ma, which is consistent with the W-rich rutile U-Pb age of 345 ± 27 Ma. These ages are considerably older than the auriferous pyrite Rb-Sr and Re-Os isochron ages of 322.5 ± 6.8 Ma (Dong et al. 2018) and 310.9 ± 4.2 Ma (Zhang et al. 2015), indicating an early Cu-Au event before the major Au mineralization event in the Katbasu deposit. In addition, the ages of the hydrothermal monazite and W-rich rutile are also consistent with the zircon U-Pb age of the diorite (352.0 ± 3.2 Ma), suggesting that the early Cu-Au mineralization may be related to diorite. This is further supported by the fact that some Cu-Au mineralization occurred in the contact area where the diorite dikes intruded into granite pluton, and the fact that Cu-Au ores are overprinted by massive Au ores (Xing et al. 2016). Thus, we consider that there was an independent ~350 Ma Cu-Au mineralization event before the ~315 Ma main mineralization event in the Katbasu deposit.

In addition to above mentioned ages, a Sm-Nd isochron age of garnet (334.3 ± 6.7 Ma; Liu et al. 2018) in skarn and an $^{40}Ar/^{39}Ar$ plateau age for sericite (268.6 ± 1.8

Ma; Gao et al. 2015) in the massive Au ore have also been reported in the Katbasu ore district. Geological characteristics show that skarn has no genetic associations with mineralization, and the Sm-Nd isochron age may represent a barren hydrothermal event in the Katbasu deposit. Given the facts that (1) the $^{40}Ar/^{39}Ar$ plateau age of sericite is much younger than that of auriferous pyrite (ca. 323-311 Ma; Zhang et al. 2015; Dong et al. 2018) in the Katbasu deposit, (2) sericite has low closure temperatures (Chiaradia et al. 2013), and (3) the Katbasu deposit has undergone multi-stage tectonic events (Zhao et al. 2019), we consider that the $^{40}Ar/^{39}Ar$ plateau age of sericite may record a post-ore tectonic thermal event in the Katbasu deposit.

6.2 Genetic type of the Katbasu Au-Cu deposit

The Chinese western Tianshan orogenic belt hosts many large epithermal gold deposits (Jinxi-Yelmand, Long et al. 2005; Axi, An and Zhu 2018) as well as orogenic gold deposits (Sawayaerdun, Chen et al. 2012; Wangfeng, Zhang et al. 2012). As a newly discovered large Au-Cu deposit in the western Tianshan, the genetic type of the Katbasu deposit remains controversial, with some researchers relating them to orogenic gold deposits (Zhang et al. 2015; Zhao et al. 2019) and others interpreting them as magmatic-hydrothermal gold deposits (Dong et al. 2018; Liu et al. 2018). The ore genesis of the Katbasu Au-Cu deposit remains debated, partly due to a lack of systematic absolute timing of the complex Au and Cu ore-forming events during the late Paleozoic orogeny in the ore district.

As discussed above, an early Cu-Au mineralization (chalcopyrite and minor native gold) and a late Au mineralization (pyrite and native gold) are the two major ore-forming events at the Katbasu deposit. Based on the available rock- and ore-forming ages in the ore district, we consider that there may be two different types of metallogenic events in the Katbasu deposit.

The formation time of Cu-Au mineralization (348.7 ± 2.3 Ma) is consistent with the emplacement age of diorite (352.0 ± 3.2 Ma) in the ore district. The Cu-Au mineralization is spatially associated with the diorite, and the diorite in the Katbasu deposit contains some disseminated chalcopyrite and pyrite (Fig. 4a), indicating that it may have provided ore-forming materials. The abundant Cu in the Cu-Au mineralization indicates that it is unlikely to be of orogenic origin because only a small portion of base metals can be released into metamorphic fluids (Zhong et al. 2015). Instead, the Cu-Au mineral assemblage is consistent with those in intrusion-related gold deposits (Sillitoe and Thompson 1998). In addition, the age of Cu-Au mineralization is also roughly consistent with the ore formation ages of the Lailisigaoer porphyry Cu-Mo deposit (Molybdenite Re-Os age of 359 ± 8 Ma; Fig. 1b; Li and Chen 2004) and the early stage of Axi epithermal Au deposit (Pyrite Re-Os age of 350 ± 10 Ma; Liu et al. 2020) in the Chinese Western Tianshan. This suggests that the early Cu-Au mineralization could have been of magmatic-hydrothermal origin. The magmatic-hydrothermal Cu-Au ores formed at ~350 Ma, corresponding to a subduction environment in the Western Tianshan (Gao et al. 2009; Feng and Zhu 2019).

By contrast, the major Au mineralization (ca. 323-311 Ma; Zhang et al. 2015; Dong et al. 2018) has no spatial associations with the diorite and it formed much later than any of the magmatic rocks in the ore district (Fig. 12), indicating that the main Au mineralization has no genetic associations with the magmatic rocks in the ore district. In addition, the Au orebodies of the Katbasu deposit is obviously controlled by a fault structure (Fig. 2b), which is consistent with the typical orogenic gold deposits (Goldfarb and Groves 2015; Taylor et al. 2021). Also, the S-Pb isotopes from the main gold ores suggest that the ore-forming metals were derived from crustal materials rather than the granite (Zhang et al. 2015). Moreover, this age is also consistent with the pyrite isochron Re-Os age of the Alastuo granitoid-hosted orogenic deposit (325 ± 3 Ma, Zu et al. 2020) in the Chinese Western Tianshan. This suggests that the main Au mineralization in the Katbasu deposit may belong to the orogenic type. The orogenic Au ores formed during ~323-311 Ma, which corresponds to the tectonic transition period from a subduction to a syn-collision environment in the Western Tianshan (Gao et al. 2009; Zu et al. 2020).

6.3 A comparison of hydrothermal monazite and rutile geochronology in the gold deposits

Monazite and rutile are common accessory minerals in different types of gold deposits, and their U-Pb isotopes are often used to determine the ore formation ages of gold mineralization (Brown et al. 2002; Sarma et al. 2008; Pereira et al. 2019).

However, there are few comparative studies on their accuracy and applicability in dating gold deposits.

In the granite-hosted Katbasu deposit, monazite and rutile coexist with chalcopyrite and native gold. The BSE images show that the monazite has a homogeneous composition (Figs. 4g and h), whereas the rutile occurs as both an early W-rich rutile and a late rutile (Figs. 10a,b). Monazite trace elements and W-rich rutile replacement textures indicate that they were both formed by hydrothermal fluids (Scott et al. 2011; Taylor et al. 2015). Although they have similar Th/U ratios, the Th and U contents of monazite are much higher than those of rutile (Table 3 and 4). In addition, the U-Pb age of monazite (348.7 ± 2.3 Ma) is consistent with, and more precise than the U-Pb age of rutile (345 ± 27 Ma). Thus, we consider that monazite is more suitable to date the complex mineralization event than rutile in the Katbasu deposit.

Other than the Katbasu deposit, the following factors indicate that monazite may be better than rutile in determining the mineralization age of other gold deposits. Rutile is one of three polymorphs, which also include anatase and brookite (Plavsa et al. 2018; Adlakha et al. 2020). In particular, the remobilization of trace elements after the formation of rutile can affect the information on the nature and timing of geological events recorded in rutile (Pe-Piper et al. 2019; Agangi et al. 2020; Verberne et al. 2020). In addition, the TiO_2 mineral polymorphs found in the gold deposits are difficult to distinguish by their geochemical compositions. Laser micro-Raman spectroscopy is a reliable technique to identify rutile (Meinhold 2010), and should be carried out before the U-Pb geochronology. Moreover, the lack of criteria for discriminating hydrothermal rutile makes it difficult to time the formation of gold deposits because rutile is a common accessory mineral in various magmatic, sedimentary, and metamorphic rocks (Zack et al. 2004; Meinhold 2010).

By contrast, monazite has no polymorphs. In addition, monazite is chemically and isotopically robust. It can incorporate significant amounts of Th and U as well as exclude common Pb, which makes it a powerful geochronometer (Spear and Pyle 2002; Rasmussen et al. 2006). Although monazite can be of magmatic, detrital, and metamorphic origins, hydrothermal monazites can be distinguished by their relatively low Th contents and Th/U ratios as well as their REE patterns (Taylor et al. 2015; Aleinikoff et al. 2016). Therefore, monazite appears to be a better geochronometer than rutile when they both appear in the same gold deposits.

7. Implications

Located in the Chinese Western Tianshan, the Katbasu Au-Cu deposit is hosted in a Carboniferous granite intrusion. The main ore types include Cu-Au ores as veinlets crosscutting the granite and Au ores with massive pyrite and quartz as major minerals. Some hydrothermal monazite and rutile grains coexist with chalcopyrite and native gold in the Cu-Au ores. Our new zircon U-Pb results show that the ore-hosting granite formed at ca. 356-354 Ma. The trace element compositions of the monazite suggest it formed from hydrothermal fluids rather than being inherited from the ore-hosting granite. The hydrothermal monazite yielded U-Pb ages of 348.7 ± 2.3 Ma and 345 ± 27 Ma, which are consistent with the zircon U-Pb age of the diorite (352.0 ± 3.2 Ma) that intruded the ore-hosting granite. These ages are much older than the auriferous pyrite (ca. 323-311 Ma) in the major Au ores, indicating an early Cu-Au mineralization event prior to the main Au mineralization. The early Cu-Au mineralization could be associated with the diorite and formed by magmatic-hydrothermal fluids. By contrast, the main Au mineralization appear to have formed by metamorphic fluids and could be classified as an orogenic deposit. The results in this study highlight that monazite has the advantages over rutile in dating the complex mineralization ages of hydrothermal gold deposits.

Acknowledgments

This research was jointly supported by the National Key Research and Development Program of China (2018YFC0603801 and 2018YFC0604004), National Natural Science Foundation of China (No. 41903042 and No. 42002052), China Postdoctoral Science Foundation (No. 2016LH0003 and No.2017M610984). We thank Ryan Taylor and anonymous reviewer(s) for their thorough and constructive reviews of this paper. Daniel Harlov is thanked for the editorial handling and language polishing.

Declaration of interests

The authors declare that they have no known competing financial interests or personal relationships that could have appeared to influence the work reported in this paper.

References

Adlakha, E. E., Hattori, K., Kerr, M. J., and Boucher B. M., (2020) The origin of Ti-oxide minerals below and within the eastern Athabasca Basin, Canada. American Mineralogist, 105(12), 1875-1888.

Agangi, A., Reddy, S. M., Plavsa, D., Fougerouse, D., Clark, C., Roberts, M., and Johnson, T. E. (2019) Antimony in rutile as a pathfinder for orogenic gold deposits. Ore Geology Reviews, 106, 1-11.

Agangi, A., Plavsa, D., Reddy, S. M., Olierook, H., and Kylander-Clark, A. (2020) Compositional modification and trace element decoupling in rutile: Insight from the Capricorn Orogen, Western Australia. Precambrian Research, 345, 105772.

Aleinikoff, J. N., Selby, D., Slack, J. F., Day, W. C., Pillers, R. M., Cosca, M. A., Seeger, C. M., Fanning, C. M., and Samson, I. M. (2016) U-Pb, Re-Os, and Ar/Ar Geochronology of Rare Earth Element (REE)-Rich Breccia Pipes and Associated Host Rocks from the Mesoproterozoic Pea Ridge Fe-REE-Au Deposit, St. Francois Mountains, Missouri. Economic Geology, 111(8), 1883-1914.

An, F., and Zhu, Y., (2018) Geology and geochemistry of the Early Permian Axi low-sulfidation epithermal gold deposit in North Tianshan (NW China). Ore Geology Reviews, 100, 12-30.

Andersen, T. (2002) Correction of common Pb in U-Pb analyses that do not report ^{204}Pb. Chemical Geology, 192, 59-79.

Bea, F. (1996) Residence of REE, Y, Th and U in granites and crustal protoliths : implications for the chemistry of crustal melts. Journal of Petrology, 37(3), 521–552.

Brown, S. M., Fletcher, I. R., Stein, H. J., Snee, L. W., and Groves, D. I. (2002) Geochronological Constraints on Pre-, Syn-, and Postmineralization Events at the World-Class Cleo Gold Deposit, Eastern Goldfields Province, Western Australia. Economic Geology, 97(3), 541-559.

Cabral, A. R., Eugster, O., Brauns, M., Lehmann, B., Rösel, D., Zack, T., de Abreu, F. R., Pernicka, E., and Barth, M. (2013) Direct dating of gold by radiogenic helium: Testing the method on gold from Diamantina, Minas Gerais, Brazil. Geology, 41(2), 163-166.

Chen, H. Y., Chen, Y. J., and Baker, M. (2012) Isotopic geochemistry of the Sawayaerdun orogenic-type gold deposit, Tianshan, northwest China: implications for ore genesis and mineral exploration. Chemical Geology, 310, 1-11.

Chiaradia, M., Konopelko, D., Seltmann, R., and Cliff, R. A., (2006) Lead isotope variations across terrane boundaries of the Tien Shan and Chinese Altay. Mineralium Deposita, 41(5), 411-428.

Chiaradia, M., Schaltegger, U., Spikings, R., Wotzlaw, J.F., and Ovtcharova, M. (2013) How accurately can we date the duration of magmatic-hydrothermal events in porphyry systems?—an invited paper. Economic Geology,108 (4), 565-584.

Cooke, D. R., Hollings, P., and Walshe, J. L. (2005) Giant porphyry deposits: characteristics, distribution, and tectonic controls. Economic Geology, 100(5), 801-818.

Deng, J., Qiu, K.F., Wang, Q.F., Goldfarb, R.J., Yang, L.Q., Zi, J.W., Geng, J.Z., and Ma, Y. (2020) In-situ dating of hydrothermal monazite and implications on the geodynamic controls of ore formation in the Jiaodong gold province, eastern China. Economic Geology, 115(3), 671-685.

Dong, L.L., Wan, B., Yang, W.Z., Deng, C., Chen, Z., Yang, L., Cai, K.D., and Xiao, W.J. (2018) Rb-Sr geochronology of single gold-bearing pyrite grains from the Katbasu gold deposit in the South Tianshan, China and its geological significance. Ore Geology Reviews, 100, 99-110.

Dostal, J., Kontak, D. J., and Chatterjee, A. K., (2009) Trace element geochemistry of scheelite and rutile from metaturbidite-hosted quartz vein gold deposits, Meguma Terrane, Nova Scotia, Canada: genetic implications. Mineralogy and Petrology, 97(1), 95-109.

Feng, B., Xue, C., Zhao, X., Ding, Z., Zhang, Q., Zu, B., Yang, W., Lin, Z., and Chen, W. (2014) Petrology, geochemistry and zircon U-Pb isotope chronology of monzogranite of the Katbasu Au-Cu deposit, western Tianshan, Xinjiang Province. Earth Science Frontiers, 21, 187-195 (in Chinese with English abstract).

Feng, W.Y., and Zhu, Y.F. (2018) Petrology and geochemistry of mafic and ultramafic rocks in the north Tianshan ophiolite: Implications for petrogenesis and tectonic setting. Lithos, 318, 124-142.

Feng, W.Y., and Zhu, Y.F. (2019) Petrogenesis and tectonic implications of the late Carboniferous calc-alkaline and shoshonitic magmatic rocks in the Awulale mountain, western Tianshan. Gondwana Research, 76, 44-61.

Fielding, I. O. H., Johnson, S. P., Zi, J. W., Rasmussen, B., Muhling, J. R., Dunkley, D. J., Sheppard, S., Wingate, M. T. D., and Rogers, J. R. (2017) Using in situ SHRIMP U-Pb monazite and xenotime geochronology to determine the age of orogenic gold mineralization: An example from the Paulsens Mine, Southern Pilbara Craton. Economic Geology, 112(5), 1205-1230.

Frimmel, H. E. (2008) Earth's continental crustal gold endowment. Earth and Planetary Science Letters, 267(1), 45-55.

Gao, J., Li, M.S., Xiao, X.C., Tang, Y.Q., and He, G.Q. (1998) Paleozoic tectonic evolution of the Tianshan Orogen, northwestern China. Tectonophysics, 287 (1-4), 213-231.

Gao, J., Long, L., Klemd, R., Qian, Q., Liu, D., Xiong, X., Su, W., Liu, W., Wang, Y.T., and Yang, F. (2009) Tectonic evolution of the South Tianshan orogen and adjacent regions, NW China: geochemical and age constraints of granitoid rocks. International Journal of Earth Sciences, 98(6), 1221-1238.

Gao, Y.W., Zhang, Z.L., Wang, Z.H., Yang, W.Z., Ban, J.Y., Dong, F.C., and Tan, W.J. (2015) Geochronology of the Katabaasu gold deposit inWest Tian Shan and its geological significance: evidence from ^{40}Ar-^{39}Ar isotopic ages of sericite. Geology and Exploration, 5, 805-815 (in Chinese with English abstract).

Goldfarb, R.J., Snee, L.W., Miller, L.D., and Newberry, R.J. (1991) Rapid dewatering of the crust deduced from ages of mesothermal gold deposits. Nature, 354 (6351), 296-298.

Goldfarb, R. J., and Groves, D. I. (2015) Orogenic gold: Common or evolving fluid and metal sources through time. Lithos, 233, 2-26.

Grosse, P., Söllner, F., Báez, M. A., Toselli, A. J., Rossi, J. N., and Rosa, J. D. de la. (2009) Lower Carboniferous post-orogenic granites in central-eastern Sierra de Velasco, Sierras Pampeanas, Argentina: U–Pb monazite geochronology, geochemistry and Sr-Nd isotopes. International Journal of Earth Sciences, 98(5), 1001-1025.

Jemielita, R. A., Davis, D. W., and Krogh, T. E. (1990) U-Pb evidence for Abitibi gold mineralization postdating greenstone magmatism and metamorphism. Nature, 346(6287), 831-834.

Kirk, J., Ruiz, J., Chesley, J., Walshe, J., and England, G. (2002) A Major Archean, Gold- and Crust-Forming Event in the Kaapvaal Craton, South Africa. Science, 297(5588), 1856-1858.

Kusiak, M. A., Williams, I. S., Dunkley, D. J., Konečny, P., Słaby, E., and Martin, H. (2014) Monazite to the rescue: U-Th-Pb dating of the intrusive history of the composite Karkonosze pluton, Bohemian Massif. Chemical Geology, 364, 76-92.

Le Mignot, E., Reisberg, L., André-Mayer, A. S., Bourassa, Y., Fontaine, A., and Miller, J. (2017) Re-Os geochronological evidence for multiple Paleoproterozoic gold events at the scale of the West African craton. Economic Geology, 112(1), 145-168.

Li, H.Q., and Chen, F.W. (2004) Isotopic, geochronology of regional mineralization in Xinjiang, China. Geological Publishing House, Beijing, 1-361 (in Chinese with English abstract).

Li, J. W., Bi, S. J., Selby, D., Chen, L., Vasconcelos, P., Thiede, D., Zhou, M.F., Zhao, X.F., Li, Z.K., and Qiu, H. N. (2012) Giant Mesozoic gold provinces related to the destruction of the North China craton. Earth and Planetary Science Letters, 349, 26-37.

Li, Q. L., Lin, W., Su, W., Li, X. H., Shi, Y. H., Liu, Y., and Tang, G. Q. (2011) SIMS U-Pb rutile age of low-temperature eclogites from southwestern Chinese Tianshan, NW China. Lithos, 122(1-2), 76-86.

Li, Q. L., Yang, Y.N., Shi, Y.H., and Lin, W. (2013) Eclogite rutile U-Pb dating: constrant for formation and evolution of continental collisional orogen. Chinese Science Bulletin, 58, 2279-2284.

Li, T., Hou, P., and Lin, L., (2018) Geological characteristics and metallogenic environment analysis of the Catabaasu gold copper Deposit: World Nonferrous Metals, 2018(12), 96-97 (in Chinese with English abstract).

Li, W., Xie, G., Mao, J., Zhu, Q., and Zheng, J. (2019) Mineralogy, Fluid Inclusion, and Stable Isotope Studies of the Chengchao Deposit, Hubei Province, Eastern

China: Implications for the Formation of High-Grade Fe Skarn Deposits. Economic Geology, 114(2), 325-352.

Li, X.H., Liu, Y., Li, Q.L., Guo, C.H., and Chamberlain, K.R. (2009) Precise determination of Phanerozoic zircon Pb/Pb age by multi-collector SIMS without external standardization. Geochemistry, Geophysics, Geosystems, 10, Q04010.

Liu, J.J., Long, X.R., Zheng, M.H., Li, E.D., Wang, J.Z., Sang, H.Q., and Yin, H.X., (2002) The metallogenic age of Sawaya'erdun gold deposit in southwestern Tianshan mountains, Xinjiang. Journal of Mineralogy and Petrology, 22 (3), 19-23 (in Chinese with English abstract).

Liu, Y., Gao, S., Hu, Z., Gao, C., Zong, K., and Wang, D. (2010) Continental and oceanic crust recycling-induced melt-peridotite interactions in the trans-North China Orogen: U–Pb dating, Hf isotopes and trace elements in zircons of mantle xenoliths. Journal of Petrology, 51, 537-571.

Liu, Y., Han, Y., Li, Z., Mo, X., Huang, Y., and Li, Y. (2018) Geological characteristics, deposit type, and metallogenic epoch of the Katebasu gold–copper deposit in western Tianshan. Geological Journal, 53, 263-277.

Liu, Z., Mao, X., Ackerman, L., Li, B., Dick, J. M., Yu, M., Peng, J.T., and Shahzad, S. M., (2020) Two-stage gold mineralization of the Axi epithermal Au deposit, Western Tianshan, NW China: Evidence from Re-Os dating, S isotope, and trace elements of pyrite. Mineralium Deposita, 55(5), 863-880.

Long, X., Hayward, N., Begg, G., Minlu, F., Fangzheng, W., and Pirajno, F. (2005) The Jinxi–Yelmand high-sulfidation epithermal gold deposit, Western Tianshan, Xinjiang Province, P.R. China. Ore Geology Reviews, 26(1), 17-37.

Ludwig, K.R. (2003) User's Manual for Isoplot 3.00 - A Geochronological Toolkit for Microsoft Excel. Berkeley Geochronology Center Special Publication. 4, 1-70.

Mao, J.W., Konopelko, D., Seltmann, R., Lehmann, B., Chen, W., Wang, Y., Eklund, O., and Usubaliev, T. (2004) Postcollisional age of the Kumtor gold deposit and timing of Hercynian events in the Tien Shan, Kyrgyzstan. Economic Geology, 99(8), 1771-1780.

Morelli, R., Creaser, R.A., Seltmann, R., Stuart, F.M., Selby, D., and Graupner, T. (2007) Age and source constraints for the giant Muruntau gold deposit, Uzbekistan, from coupled Re-Os-He isotopes in arsenopyrite: Geology, 35 (9), 795-798.

Meinhold, G. (2010) Rutile and its applications in earth sciences. Earth-Science Reviews, 102(1-2), 1-28.

Pe-Piper, G., Nagle, J., Piper, D. J. W., and McFarlane, C. R. M. (2019). Geochronology and trace element mobility in rutile from a Carboniferous syenite pegmatite and the role of halogens. American Mineralogist, 104(4), 501-513.

Pereira, I., Storey, C. D., Darling, J., Lana, C. de C., and Alkmim, A. R. (2019) Two billion years of evolution enclosed in hydrothermal rutile: Recycling of the São Francisco Craton Crust and constraints on gold remobilisation processes. Gondwana Research, 68, 69-92.

Piechocka, A. M., Gregory, C. J., Zi, J. W., Sheppard, S., Wingate, M. T. D., and Rasmussen, B. (2017) Monazite trumps zircon: applying SHRIMP U–Pb geochronology to systematically evaluate emplacement ages of leucocratic, low-temperature granites in a complex Precambrian orogeny. Contributions to Mineralogy and Petrology, 172(8), 63.

Plavsa, D., Reddy, S. M., Agangi, A., Clark, C., Kylander-Clark, A., and Tiddy, C. J. (2018) Microstructural, trace element and geochronological characterization of TiO_2 polymorphs and implications for mineral exploration: Chemical Geology, 476, 130-149.

Rasmussen, B., Fletcher, I. R., Sheppard, S. (2005). Isotopic dating of the migration of a low-grade metamorphic front during orogenesis. Geology, 33(10), 773-776.

Rasmussen, B., Sheppard, S., and Fletcher, I. R. (2006) Testing ore deposit models using in situ U-Pb geochronology of hydrothermal monazite: Paleoproterozoic gold mineralization in northern Australia. Geology, 34(2), 77-80.

Sarma, D. S., Mcnaughton, N., Fletcher, I. R., Groves, D., Mohan, M. R., and Balaram, V. (2008) Timing of gold mineralization in the Hutti gold deposit, Dharwar Craton, South India. Economic Geology, 103(8), 1715-1727.

Schandl E. S., and Gorton M. P. (2004) A textural and geochemical guide to the identification of hydrothermal monazite: criteria for selection of samples for dating epigenetic hydrothermal ore deposits. Economic Geology, 99, 1027-1035.

Scott, K., Radford, N., Hough, R. M., and Reddy, S. M. (2011) Rutile compositions in the Kalgoorlie Goldfields and their implications for exploration. Australian Journal of Earth Sciences, 58(7), 803-812.

Selby, D., Creaser, R. A., Hart, C. J. R., Rombach, C. S., Thompson, J. F. H., Smith, M. T., Bakke, A. A., and Goldfarb, R. J. (2002) Absolute timing of sulfide and gold mineralization: A comparison of Re-Os molybdenite and Ar-Ar mica methods from the Tintina Gold Belt, Alaska. Geology, 30(9), 791-794.

Sláma, J., Košler, J., Condon, D.J., Crowley, J.L., Gerdes, A., Hanchar, J.M., Horstwoodd, M.S.A., Morrish, G.A., Nasdalai, L., Norbergi, N., and Schaltegger, U. (2008) Plešovice zircon-a new natural reference material for U-Pb and Hf isotopic microanalysis: Chemical Geology, 249, 1-35.

Sillitoe, R. H., and Thompson, J. F. H. (1998) Intrusion-Related Vein Gold Deposits: Types, Tectono - Magmatic Settings and Difficulties of Distinction from Orogenic Gold Deposits. Resource Geology, 48(4), 237-250.

Spear, F.S., and Pyle, J.M. (2002) Apatite, monazite, and xenotime in metamorphic rocks: Geochemical, geobiological, and materials importance. Reviews in Mineralogy and Geochemistry, 48, 293-335.

Stacey, J.S., and Kramers, J.D. (1975) Approximation of terrestrial lead isotope evolution by a two-stage model. Earth and Planetary Science Letters, 26, 207-221.

Steiger, R. H., and Jäger, E. (1977) Subcommission on geochronology: Convention on the use of decay constants in geo- and cosmochronology. Earth and Planetary Science Letters, 36(3), 359-362.

Stein, H. J., Morgan, J. W., and Scherstén, A. (2000) Re-Os Dating of Low-Level Highly Radiogenic (LLHR) Sulfides: The Harnäs Gold Deposit, Southwest Sweden, Records Continental-Scale Tectonic Events. Economic Geology, 95(8), 1657-1671.

Stein, H. J. (2014) Dating and Tracing the History of Ore Formation. Treatise on Geochemistry, 13, 87-118.

Taylor, R. D., Goldfarb, R. J., Monecke, T., Fletcher, I. R., Cosca, M. A., and Kelly, N. M. (2015) Application of U-Th-Pb Phosphate Geochronology to Young Orogenic Gold Deposits: New Age Constraints on the Formation of the Grass Valley Gold District, Sierra Nevada Foothills Province, California. Economic Geology, 110(5), 1313-1337.

Taylor, R. D., Monecke, T., Reynolds, T. J., and Monecke, J. (2021) Paragenesis of an Orogenic Gold Deposit: New Insights on Mineralizing Processes at the Grass Valley District, California. Economic Geology, 116(2), 323-356.

Triebold, S., Luvizotto, G. L., Tolosana-Delgado, R., Zack, T., and Eynatten, H. von. (2011) Discrimination of TiO_2 polymorphs in sedimentary and metamorphic rocks. Contributions to Mineralogy and Petrology, 161(4), 581–596.

Verberne, R., Reddy, S. M., Saxey, D. W., Fougerouse, D., Rickard, W. D. A., Plavsa, D., Agangi, A., and Kylander-Clark, A. R. C. (2020) The geochemical and geochronological implications of nanoscale trace-element clusters in rutile. Geology, 48(11), 1126-1130.

Villa, I. M., and Hanchar, J. M. (2017). Age discordance and mineralogy. American Mineralogist, 102(12), 2422-2439.

White, N. C. (2007) Exploring in China: the challenges and rewards. SEG Newsletter, 70(1), 8-15.

Xing, L., Zang, M., Yang, W.Z., Song, A., Lin, Z.H., Chen, W., and Ma, Y. (2016). Discovery of the mineralization diorite in Katebaasu gold-copper deposit, Xinjiang and its geological significance. Xinjiang Geology, 34(2), 211-217 (in Chinese with English abstract).

Xing, L., Xue, C., Zang, M., Yang, W.Z., Zhao, X., Song, A., Lin, Z.H., Zhang, Q., and Feng, B. (2018) Element distribution of Katebasu gold-copper deposit in West Tianshan Mountains and its exploration significance. Mineral Deposits, 37(1), 105-115 (in Chinese with English abstract).

Xue, C.J., Zhao, X.B., Mo, X.X., Dong, L.H., Gu, X.X., Nurtaev, B., Pak, N., Zhang, Z.C., and Wang, X. (2014) Asian Gold Belt in western Tianshan and its dynamic settings, metallogenic control and exploration: Earth Science Frontiers, 21, 128-155 (in Chinese with English abstract).

Yang, W., Xue, C., Zhao, X., Zhao, S., Wei, J., Feng, B., Zhou, H., Lin, Z., Zheng, H., Liu, J., Zhang, Q., and Zu, B. (2013) The discovery of the Kateba'asu large Au-Cu deposit in Xinyuan County, western Tianshan, Xinjiang: Geological Bulletin of China, 32, 1613-1620 (in Chinese with English abstract).

Yakubchuk, A.S., Shatov, V.V., Kirwin, D., Tomurtogoo, O., Badarch, G., and Buryak, A.A., (2005) Gold and base metal metallogeny of the central Asian orogenic supercollage. Economic Geology 100th Anniversary Volume. 1035-1068.

Zack, T., Eynatten, H. von, and Kronz, A. (2004) Rutile geochemistry and its potential use in quantitative provenance studies. Sedimentary Geology, 171(1), 37-58.

Zhai, D., Williams-Jones, A. E., Liu, J., Selby, D., Li, C., Huang, X.-W., Qi, L., and Guo, D. (2019) Evaluating the Use of the Molybdenite Re-Os Chronometer in Dating Gold Mineralization: Evidence from the Haigou Deposit, Northeastern China. Economic Geology, 114(5), 897-915.

Zhai, W., Sun, X., Sun, W., Su, L., He, X., and Wu, Y. (2009) Geology, geochemistry, and genesis of Axi: A Paleozoic low-sulfidation type epithermal gold deposit in Xinjiang, China. Ore Geology Reviews, 36(4), 265-281.

Zhang, L., Chen, H., Chen, Y., Qin, Y., Liu, C., Zheng, Y., and Jansen, N. H. (2012) Geology and fluid evolution of the Wangfeng orogenic-type gold deposit, Western Tian Shan, China. Ore Geology Reviews, 49, 85-95.

Zhang, Q., Xue, C., Zhao, X., Feng, B., Xing, H., Mo, X., Zhao, S., Yang, W., and Xing, L. (2015) Geology, geochemistry, and metallogenic epoch of the Katebasu large-sized gold deposit, Western Tianshan Mountains, Xinjiang. Geology in China, 42, 411-438 (in Chinese with English abstract).

Zhao, W., Zhao, X., Xue, C., Symons, D. T. A., Cui, X., and Xing, L. (2019) Structural characterization of the Katebasu gold deposit, Xinjiang, China: Tectonic correlation with the amalgamation of the western Tianshan. Ore Geology Reviews, 107, 888-902.

Zheng, J.H., Mao, J.W., Yang, F.Q., Chai, F.M., and Liu, F. (2016) Newly discovered native gold and bismuth in the Cihai iron-cobalt deposit, eastern Tianshan, Northwest China: Acta Geological Sinica-English Edition, 90(3), 928-938.

Zheng, J.H., Shen, P., and Li, C.H. (2020) Ore genesis of Axi post-collisional epithermal gold deposit, western Tianshan, NW China: Constraints from U–Pb dating, Hf isotopes, and pyrite in situ sulfur isotopes. Ore Geology Reviews, 117, 103290.

Zhong, R., Brugger, J., Tomkins, A. G., Chen, Y., and Li, W. (2015) Fate of gold and base metals during metamorphic devolatilization of a pelite. Geochimica et Cosmochimica Acta, 171, 338-352.

Zhu, Y.F., Guo, X., Song, B., Zhang, L.F., and Gu, L.B. (2009) Petrology, Sr–Nd–Hf isotopic geochemistry and zircon chronology of the Late Palaeozoic volcanic rocks in the southwestern Tianshan Mountains, Xinjiang, NW China. Journal of the Geological Society, 166(6), 1085-1099.

Zhu, Y.F. (2011) Zircon U-Pb and muscovite $^{40}Ar/^{39}Ar$ geochronology of the gold-bearing Tianger mylonitized granite, Xinjiang, northwest China: Implications for radiometric dating of mylonitized magmatic rocks. Ore Geology Reviews, 40(1), 108-121.

Zhu, Y.F., An, F., Feng, W.Y., and Zhang, H.C. (2016) Geological evolution and huge ore-forming belts in the core part of the Central Asian Metallogenic region. Journal of Earth Science, 27, 491-506.

Zi, J.W., Rasmussen, B., Muhling, J. R., Fletcher, I. R., Thorne, A. M., Johnson, S. P., Cutten, H, N., Dunkley, D. J., and Korhonen, F. J. (2015) In situ U-Pb geochronology of xenotime and monazite from the Abra polymetallic deposit in the Capricorn Orogen, Australia. Dating hydrothermal mineralization and fluid flow in a long-lived crustal structure: Precambrian Research, 260, 91-112.

Zu, B., Xue, C., Seltmann, R., Dolgopolova, A., Chi, G., and Li, C. (2020) Geology, geochronology, and S-Pb-Os geochemistry of the Alastuo gold deposit, West Tianshan, NW China. Mineralium Deposita, 55(7), 1-18.

Figure Captions

Figure 1. (a) Simplified geological map of the Tianshan orogenic belt showing the main tectonic units and gold deposits (modified from Mao et al. 2004; Yakubchuk et al. 2005; Xue et al. 2014). (b) Simplified geological map of the Chinese Western Tianshan showing the main tectonic units as well as iron, copper, and gold deposits (modified from Zheng et al. 2020).

Figure 2. Geological characteristics of the Katbasu Au-Cu deposit in the Western Tianshan (modified from Yang et al. 2013). (a) Regional geological map of the

Katbasu Au-Cu deposit. (b) Geological map showing the distributions of orebodies, magmatic rocks and strata in the Katbasu Au-Cu deposit. (c) Cross-section diagram of the representative exploration line of the Katbasu gold deposit.

Figure 3. Representative photos showing major types of rocks and ores in the Katbasu Au-Cu deposit. (a) Hand specimen of granite, which consists of potassium feldspar, quartz, plagioclase, and biotite. (b) Hand specimen of mafic enclave in the granite. The mafic enclaves have relatively homogenous mineral sizes and textures from their rims to cores. (c) Hand specimen of diorite, which consists mainly of plagioclase and amphibole. (d) Disseminated pyrite in the hydrothermally altered granite. (e) Pyrite-chalcopyrite veins, associated with chlorite and sericite alterations, crosscut the granite. (f) The granite was replaced by pyrite-quartz veins. (g) Pyrite-quartz vein in the massive sulfide ore. (h) Massive sulfide ore consisting mainly of pyrite and minor quartz. (i) Post-ore calcite veins that crosscut the Au mineralization with a small amount of disseminated pyrites.

Mineral abbreviations: Py = pyrite, Cpy = chalcopyrite, Qtz = quartz, Cc = calcite.

Figure 4. Representative photomicrographs and BSE images of rutile, monazite, and ore minerals in the Katbasu Au-Cu deposit. (a) Amphibole, plagioclase, magnetite, and disseminated pyrite and chalcopyrite in the diorite, reflected light. (b) and (c) Rutile coexists with chalcopyrite in the Cu-Au ores, reflected light. (d) Disseminated pyrite (Py1) in the granite. The pyrite shows a homogeneous texture without zoning,

and it has no genetic associations to the gold or copper minerals. (e) Pyrite (Py2), chalcopyrite, and native gold in the sulfide veins that crosscut the granite. (f) Chalcopyrite grains coexist with native gold grains. (g) and (h) Intergrowth of chalcopyrite and monazite in sulfide veins. (i) Pyrite (Py3), scheelite, apatite, and quartz in massive ores. Apatite crystals are not visible because of the brightness and contrast settings.

Mineral abbreviations: Py = pyrite, Cpy = chalcopyrite, Pl = plagioclase, Amp = amphibole, Mt = magnetite, Rt = rutile, Au = native gold, Mnz = monazite, Sch = scheelite, Ap = apatite, Qtz = quartz.

Figure 5. Representative BSE images of ore minerals in the Katbasu Au-Cu deposit. (a) Pyrite, chalcopyrite, native gold, and Te-Bi minerals in the Au-Cu ores. Native gold and Te-Bi minerals occur in the chalcopyrite veins. (b) A close-up view of tetradymite in the chalcopyrite vein in the Fig.a. (c) A close-up view of native gold in the chalcopyrite vein in Fig. 5a. (d) A close-up view of hessite and petzite in the chalcopyrite vein in Fig. 5a. (e) Pyrite (Py3), scheelite, and quartz in massive Au ores. The composition of the pyrite is homogeneous without obvious zoning. (f) Disseminated pyrite (Py4) in post-ore calcite veins.

Mineral abbreviations: Py = pyrite, Cpy = chalcopyrite, Au = native gold, Sch = scheelite, Qtz = quartz.

Figure 6. A mineral association diagram of the Katbasu Au-Cu mineralization. The

line thickness represents the relative abundance of minerals.

Figure 7. SIMS zircon U-Pb concordia diagrams for granite (a) and mafic enclave (b) from the Katbasu Au-Cu deposit.

Figure 8. (a) LA-ICP-MS U-Pb age of diorite in the Katbasu Au-Cu deposit. Combined with the geological fact that diorite intruded into granite and the crystallization age of the granite is ~ 356 Ma, the zircon older than 356 Ma in the diorite is considered to be xenocrystic zircon captured from the strata during its ascending process. Therefore, only zircons with ages of less than 356 Ma in figure 8c and 8d represent the crystallization age of diorite. Because the rim is too thin to be analyzed, we only analyzed the cores. (b) The weighted mean $^{206}Pb/^{238}U$ age of inherited zircon grains in the diorite. (c) The concordia diagram for magmatic zircon grains from the diorite. (d) The weighted mean $^{206}Pb/^{238}U$ age of the magmatic zircon grains from the diorite.

Figure 9. (a) Concentrations of Th versus Th/U ratios for monazite grains that coexist with chalcopyrite from the Katbasu Au-Cu deposit. No magmatic monazite was found in the granite. The hydrothermal and igneous monazite data are from Taylor et al. (2015). (b) The contents of Th versus U for monazite from the Katbasu Au-Cu deposit. The hydrothermal monazite data are from Rasmussen et al. (2005) and Zi et al. (2015), and the magmatic monazite data are from Bea (1996), Grosse et al. (2009), Kusiak et

DOI: https://doi.org/10.2138/am-2022-8080. http://www.minsocam.org/

al. (2014), and Piechocka et al. (2017). (c) The concordia diagram for hydrothermal monazite from the Katbasu deposit. (d) The weighted mean $^{206}Pb/^{238}U$ age of hydrothermal monazite from the Katbasu deposit.

Figure 10. (a) and (b) Representative BSE images of early formed W-rich rutile grains (Rt1) and later formed rutile grains (Rt2) that coexist with chalcopyrite in the Katbasu Au-Cu deposit. (c) Raman spectra of Rt1 and Rt2 from the Katbasu Au-Cu deposit. (d) Comparison of Raman spectra among the brookite, anatase, and rutile (Meinhold, 2010).

Figure 11. A Tera-Wasserburg plot for U-Pb data from W-rich rutile grains from the Katbasu Au-Cu deposit.

Figure 12. A summary of the timing of mineralization, hydrothermal alteration, and magmatism in the Katbasu ore field. In addition to the age data from this study, other age data are from Zhang et al. (2014), Gao et al. (2015), Zhang et al. (2015), Dong et al. (2018), Li et al., (2018), and Liu et al. (2018).

Table Captions

Table 1. Zircon SIMS U-Pb isotopic results for the Katbasu granite and mafic enclave.

Table 2. Results from LA-MC-ICP MS zircon U-Pb dating of diorite in the Katbasu Au-Cu deposit.

Table 3. Results from LA-MC-ICP MS U-Pb dating of hydrothermal monazites in the Katbasu Au-Cu deposit.

Table 4. Results from SIMS U-Pb dating of W-rich rutile in the Katbasu Au-Cu deposit.

Figure 1

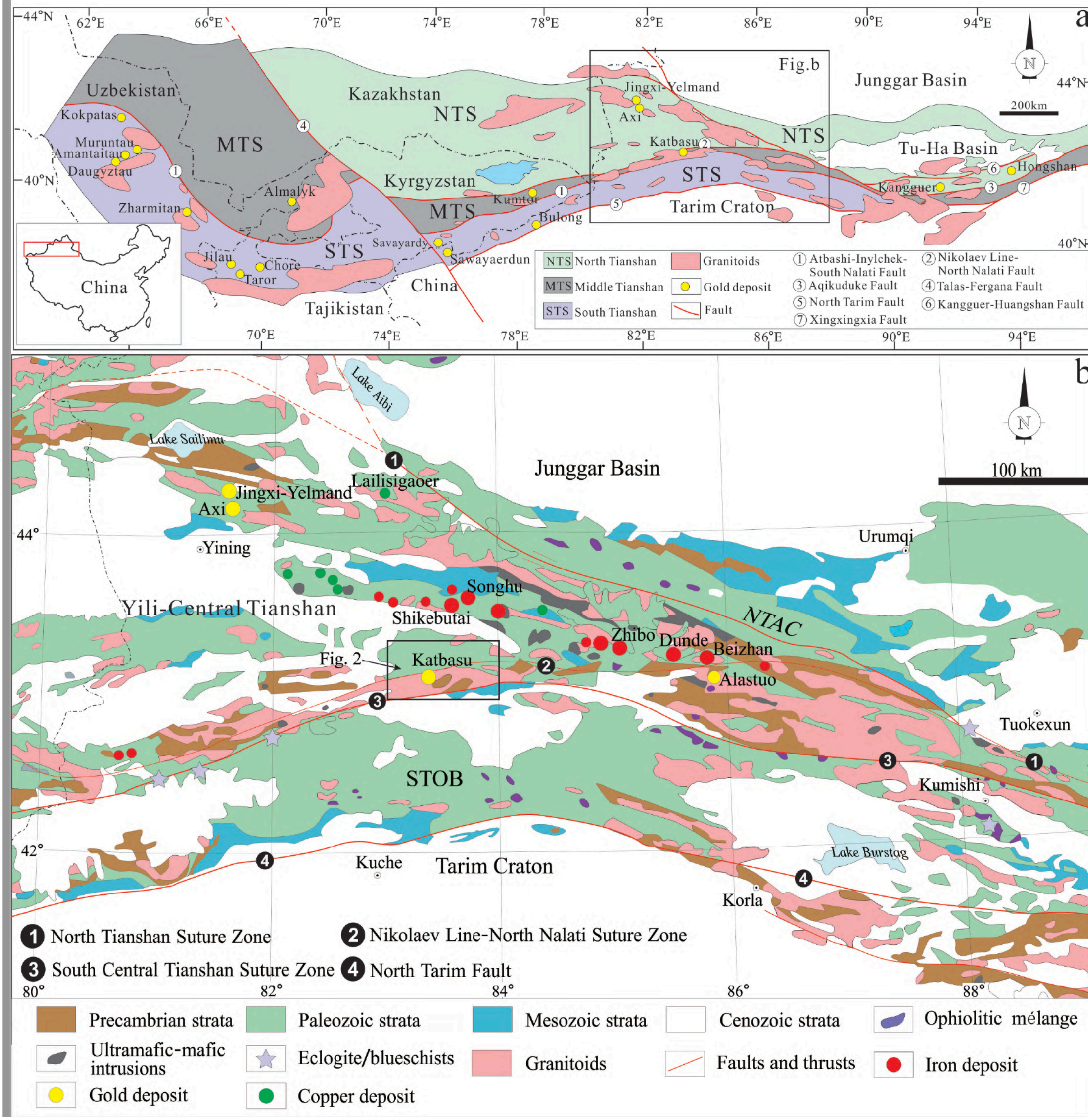

a
Fig.b
Uzbekistan
Kazakhstan
Kyrgyzstan
Tajikistan
China
NTS
MTS
STS
Junggar Basin
Tu-Ha Basin
Tarim Craton
200km
Kokpatas
Muruntau
Amantaitau
Daugyztau
Zharmitan
Almalyk
Jilau
Chore
Taror
Savayardy
Sawayaerdun
Kumtor
Bulong
Jingxi-Yelmand
Axi
Katbasu
Kangguer
Hongshan
NTS North Tianshan
MTS Middle Tianshan
STS South Tianshan
Granitoids
Gold deposit
Fault
① Atbashi-Inylchek-South Nalati Fault
② Nikolaev Line-North Nalati Fault
③ Aqikuduke Fault
④ Talas-Fergana Fault
⑤ North Tarim Fault
⑥ Kangguer-Huangshan Fault
⑦ Xingxingxia Fault
b
Lake Aibi
Lake Sailimu
Junggar Basin
100 km
Lailisigaoer
Jingxi-Yelmand
Axi
Yining
Urumqi
Yili-Central Tianshan
Songhu
Shikebutai
NTAC
Zhibo
Dunde
Beizhan
Fig. 2
Katbasu
Alastuo
Tuokexun
STOB
Kumishi
Lake Burstag
Kuche
Tarim Craton
Korla
❶ North Tianshan Suture Zone
❷ Nikolaev Line-North Nalati Suture Zone
❸ South Central Tianshan Suture Zone
❹ North Tarim Fault
Precambrian strata
Paleozoic strata
Mesozoic strata
Cenozoic strata
Ophiolitic mélange
Ultramafic-mafic intrusions
Eclogite/blueschists
Granitoids
Faults and thrusts
Iron deposit
Gold deposit
Copper deposit

Figure 2

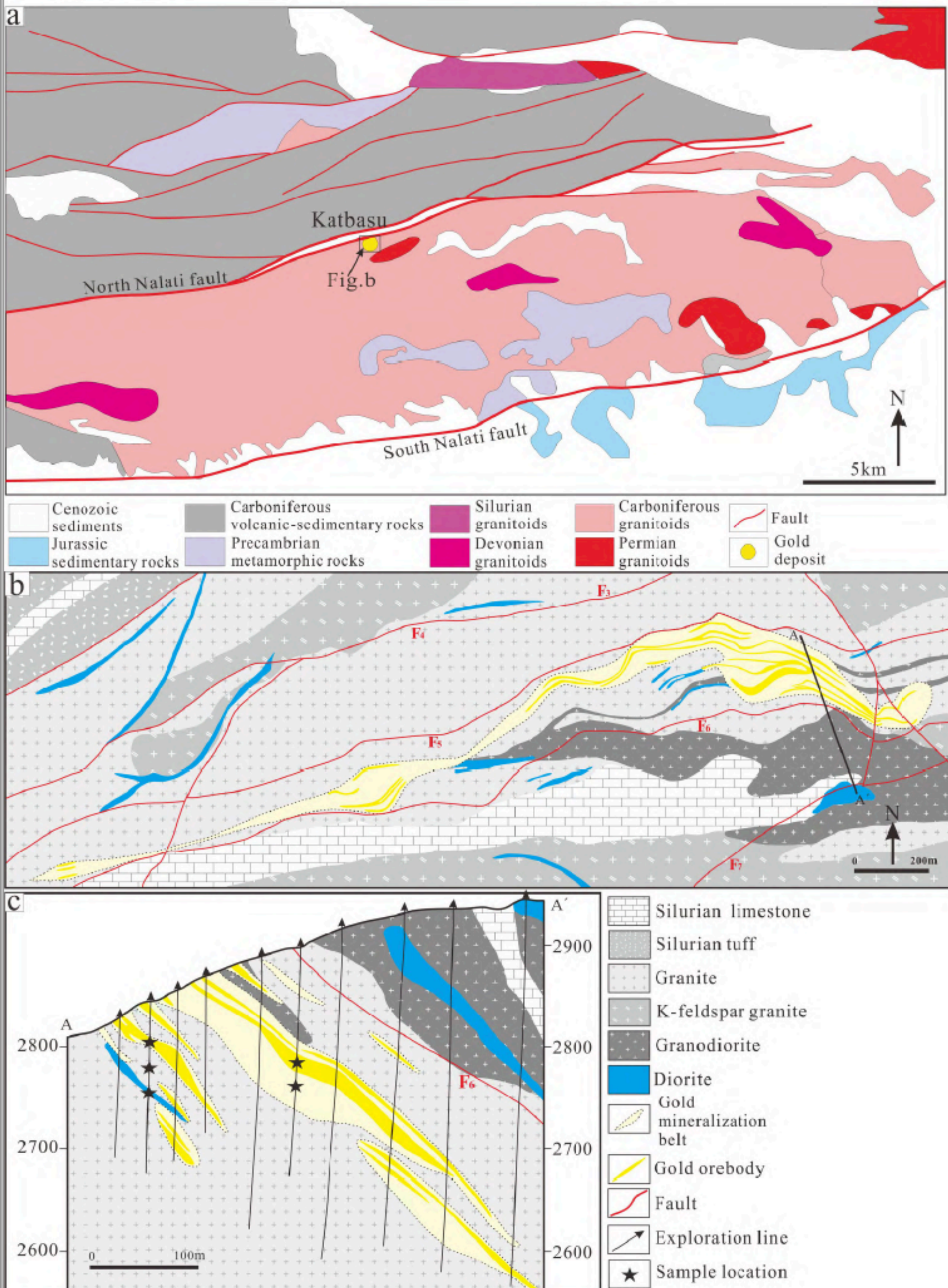

a
Katbasu
Fig.b
North Nalati fault
South Nalati fault
N
5km
Cenozoic sediments
Jurassic sedimentary rocks
Carboniferous volcanic-sedimentary rocks
Precambrian metamorphic rocks
Silurian granitoids
Devonian granitoids
Carboniferous granitoids
Permian granitoids
Fault
Gold deposit
b
F3
F4
F5
F6
F7
A
A′
N
0
200m
c
A
A′
2900
2800
2700
2600
F6
0
100m
Silurian limestone
Silurian tuff
Granite
K-feldspar granite
Granodiorite
Diorite
Gold mineralization belt
Gold orebody
Fault
Exploration line
Sample location

Figure 3

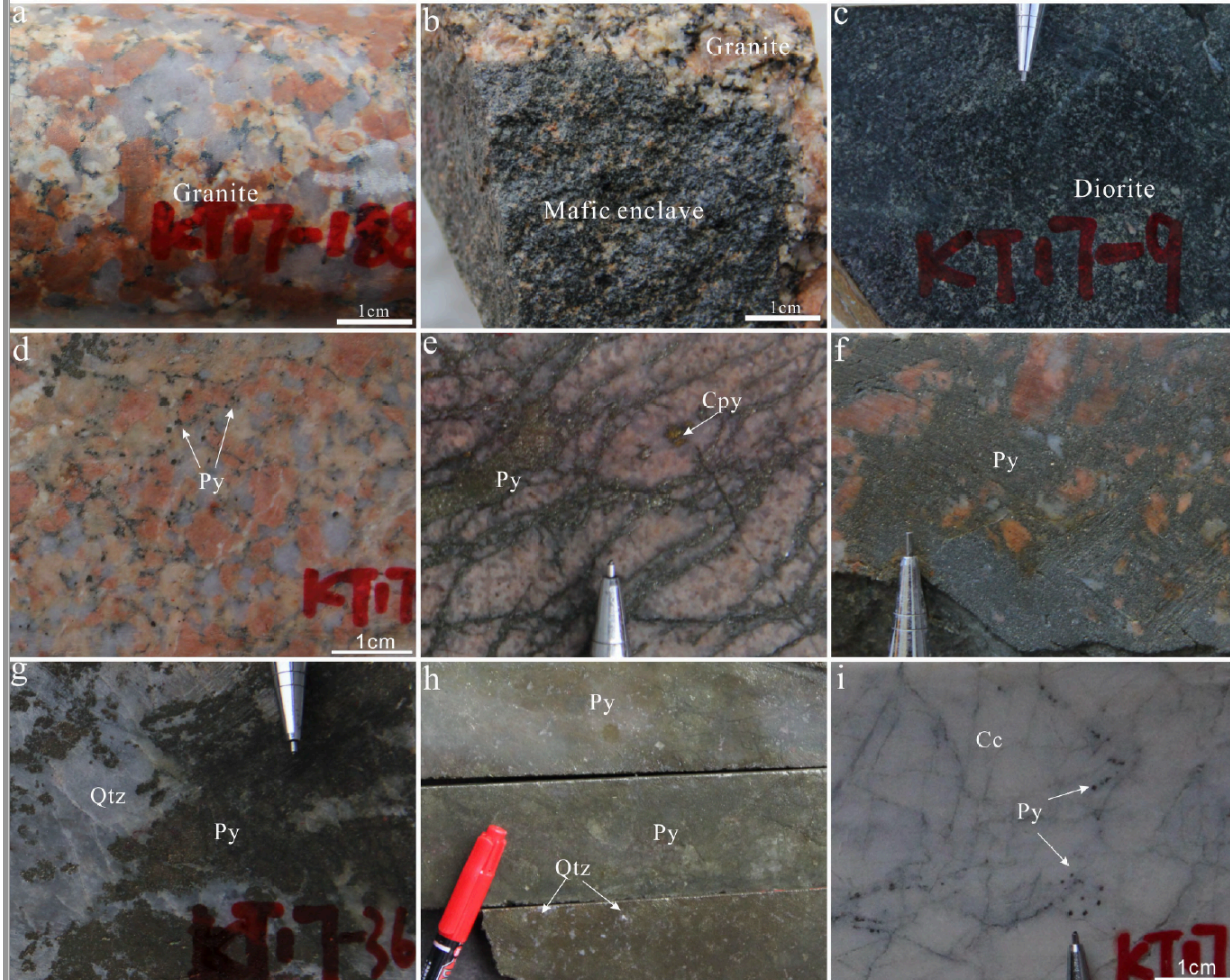
a
Granite
KT17-188
1cm
b
Granite
Mafic enclave
1cm
c
Diorite
KT17-9
d
Py
KT17
1cm
e
Cpy
Py
f
Py
g
Qtz
Py
KT17-36
h
Py
Py
Qtz
i
Cc
Py
1cm

Figure 4

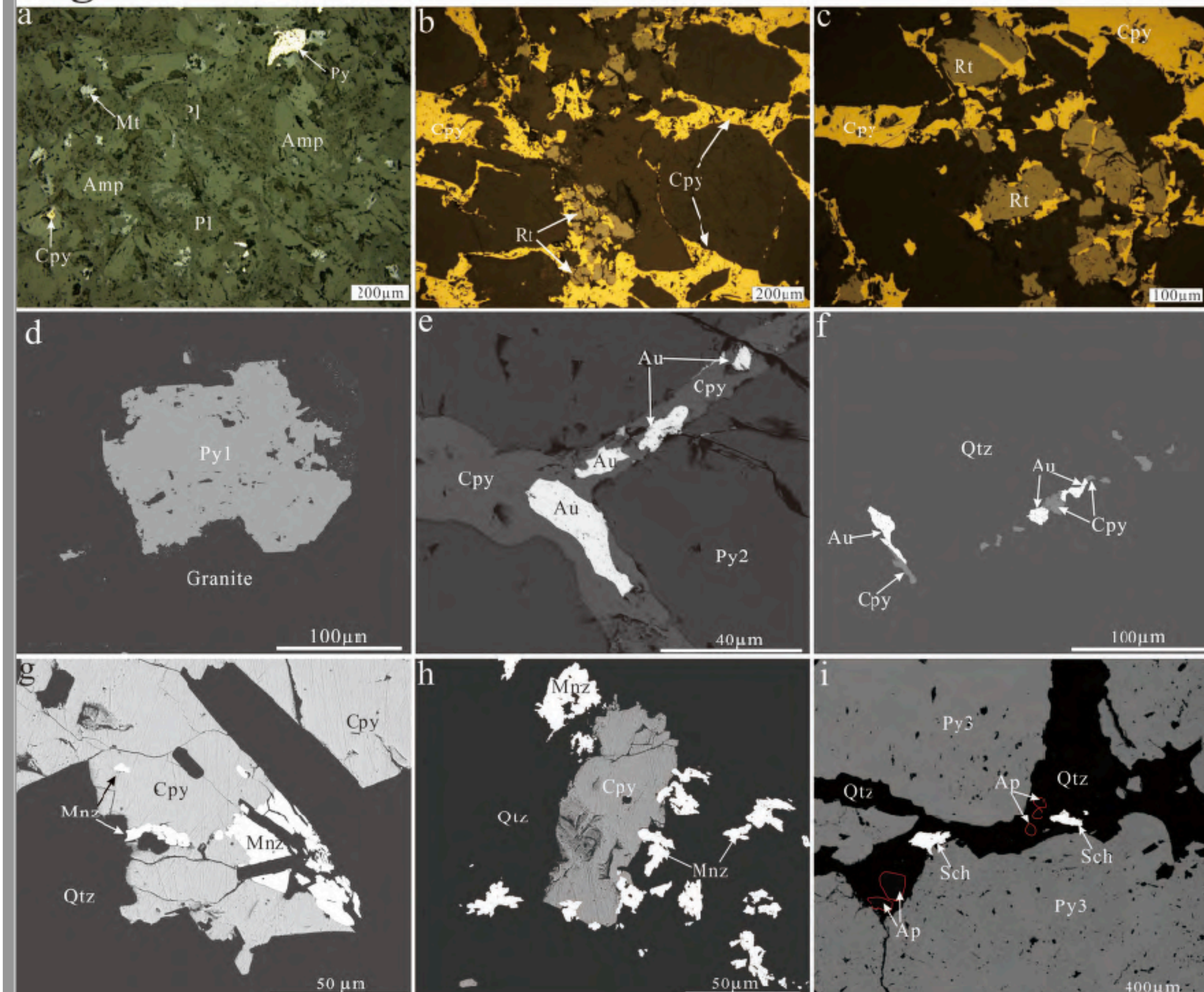

a
Py
Mt
Pl
Amp
Amp
Pl
Cpy
200μm
b
Cpy
Cpy
Rt
200μm
c
Cpy
Rt
Cpy
Rt
100μm
d
Py1
Granite
100μm
e
Au
Cpy
Au
Cpy
Au
Py2
40μm
f
Qtz
Au
Au
Cpy
Cpy
100μm
g
Cpy
Cpy
Mnz
Mnz
Qtz
50 μm
h
Mnz
Cpy
Qtz
Mnz
50μm
i
Py3
Qtz
Ap
Qtz
Sch
Sch
Py3
Ap
400μm

Figure 5

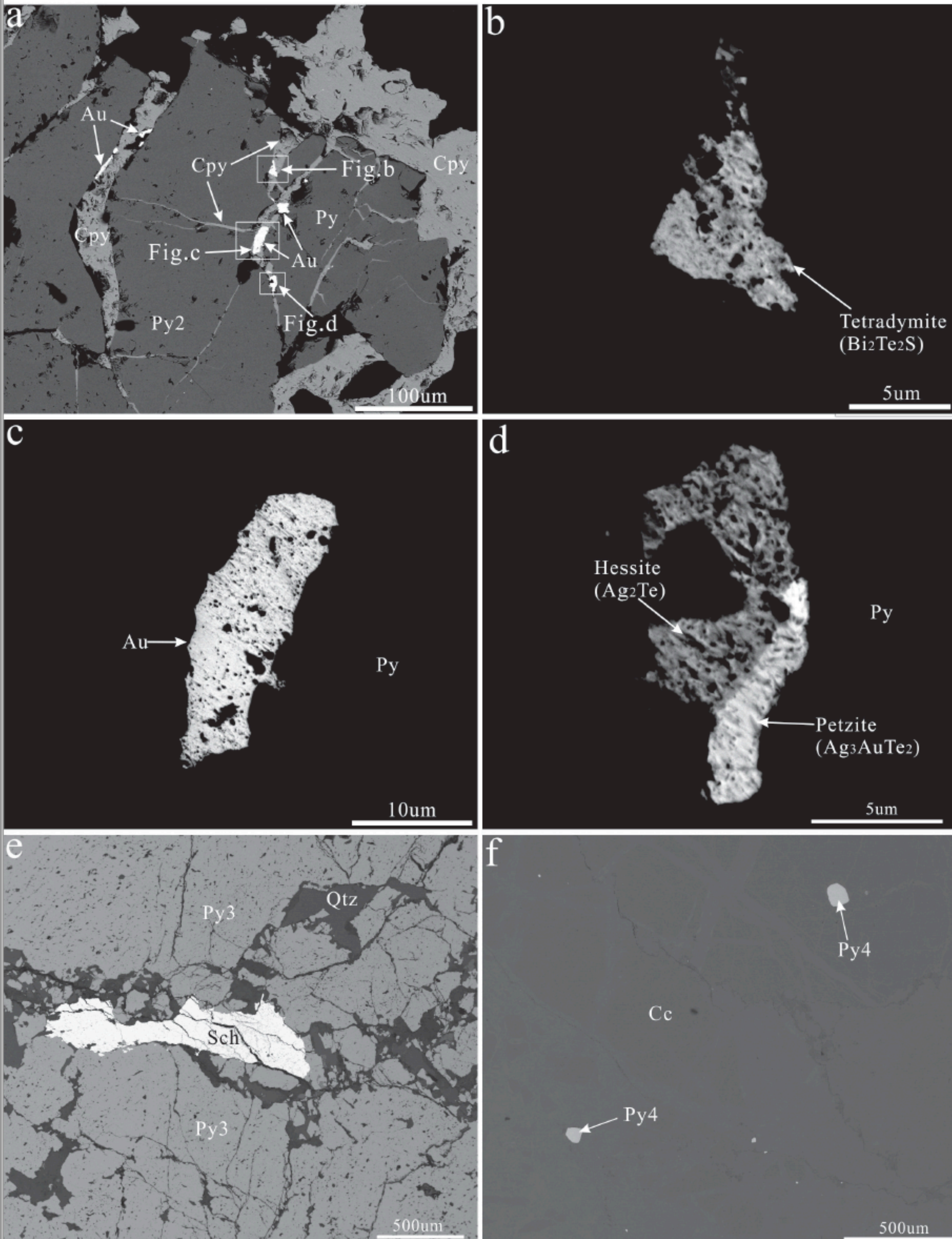
a
Au
Cpy
Fig.b
Cpy
Py
Cpy
Fig.c
Au
Au
Py2
Fig.d
100um
b
Tetradymite
(Bi2Te2S)
5um
c
Au
Py
10um
d
Hessite
(Ag2Te)
Py
Petzite
(Ag3AuTe2)
5um
e
Py3
Qtz
Sch
Py3
500um
f
Py4
Cc
Py4
500um

Figure 6

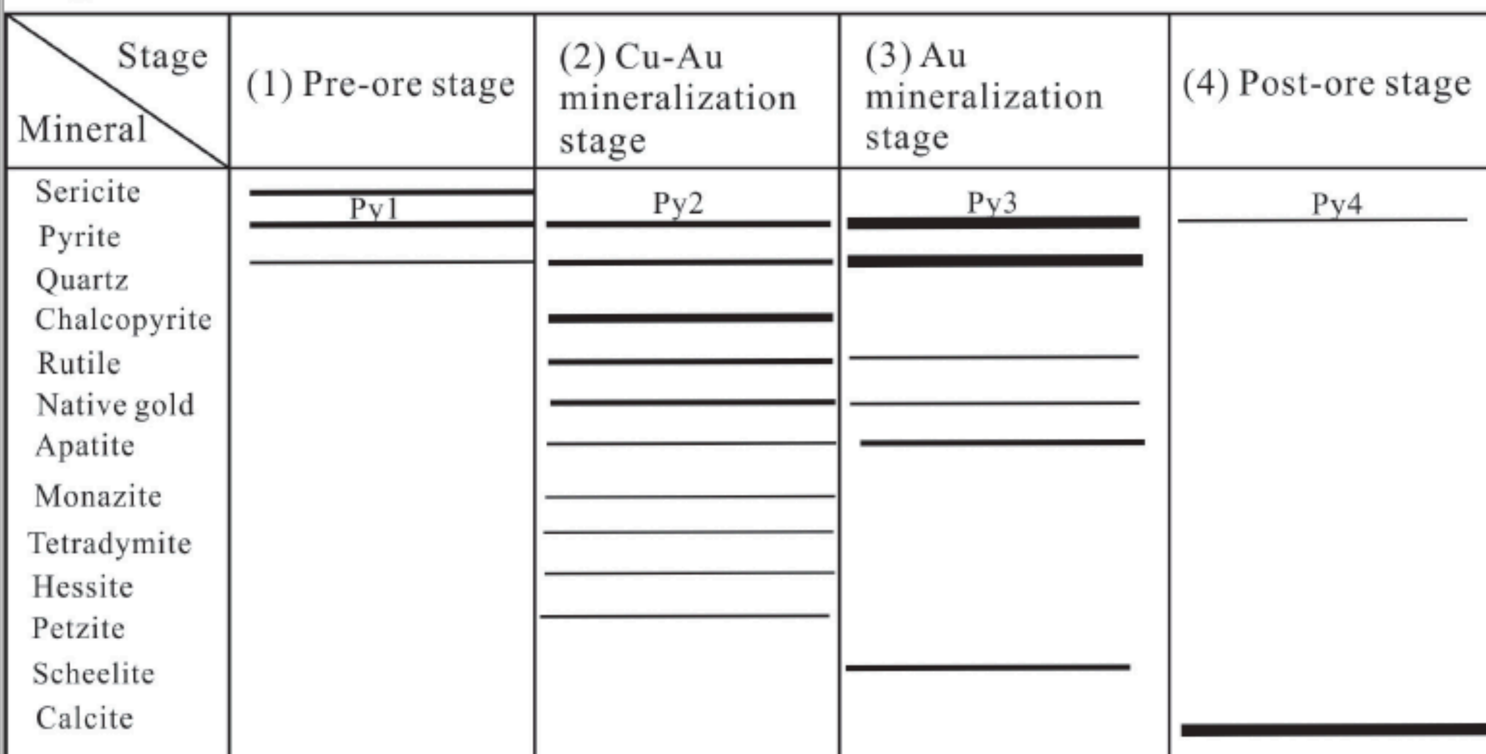
Stage
Mineral
(1) Pre-ore stage
(2) Cu-Au mineralization stage
(3) Au mineralization stage
(4) Post-ore stage
Sericite
Pyrite
Quartz
Chalcopyrite
Rutile
Native gold
Apatite
Monazite
Tetradymite
Hessite
Petzite
Scheelite
Calcite
Py1
Py2
Py3
Py4

Figure7

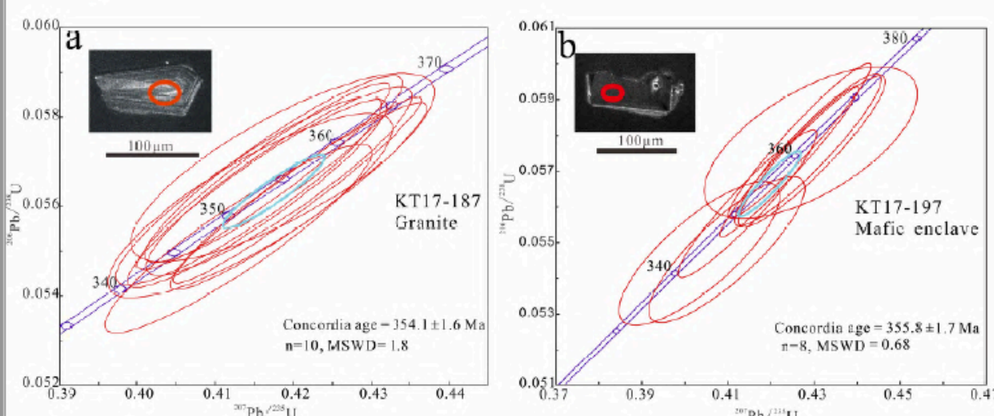
a
100μm
KT17-187
Granite
Concordia age = 354.1±1.6 Ma
n=10, MSWD= 1.8
b
100μm
KT17-197
Mafic enclave
Concordia age = 355.8±1.7 Ma
n=8, MSWD = 0.68

Figure 8

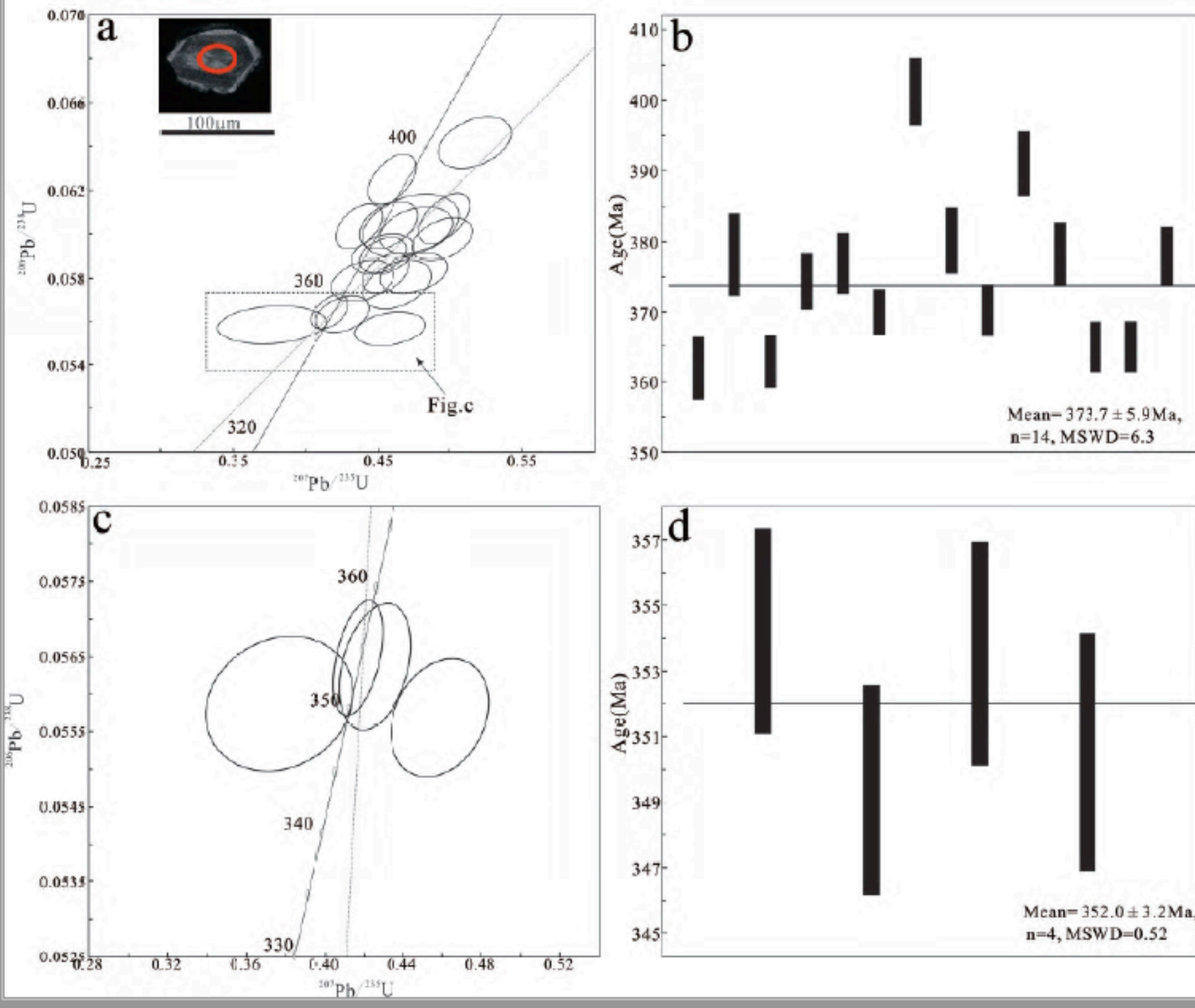
a
100μm
400
360
320
Fig.c
$^{206}Pb/^{238}U$
$^{207}Pb/^{235}U$
b
Age(Ma)
Mean= 373.7 ± 5.9Ma,
n=14, MSWD=6.3
c
360
350
340
330
$^{206}Pb/^{238}U$
$^{207}Pb/^{235}U$
d
Age(Ma)
Mean= 352.0 ± 3.2Ma,
n=4, MSWD=0.52

Figure 9

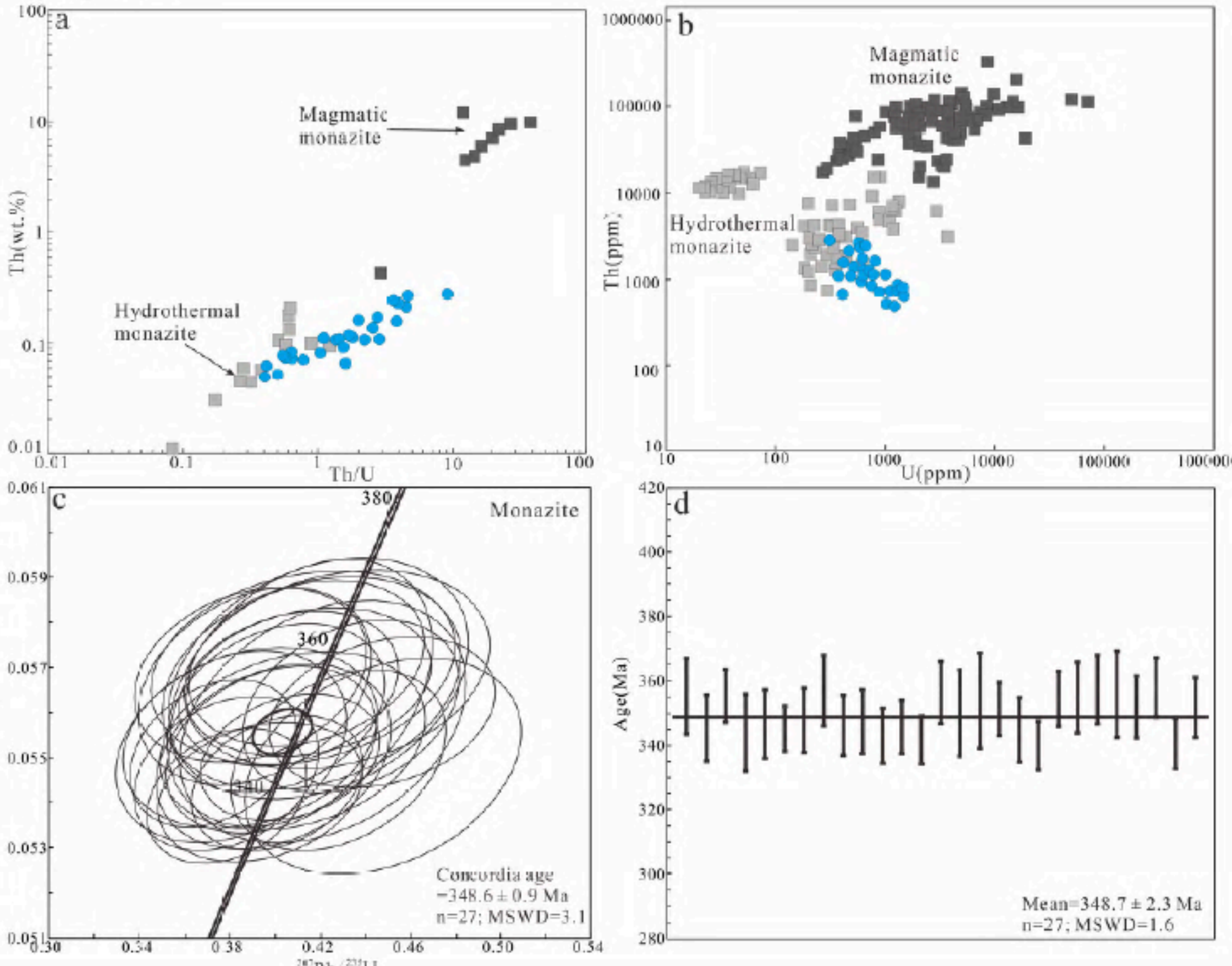
a
Magmatic monazite
Hydrothermal monazite
Th(wt.%)
Th/U
b
Magmatic monazite
Hydrothermal monazite
Th(ppm)
U(ppm)
c
Monazite
Concordia age
=348.6 ± 0.9 Ma
n=27; MSWD=3.1
d
Age(Ma)
Mean=348.7 ± 2.3 Ma
n=27; MSWD=1.6

Figure 10

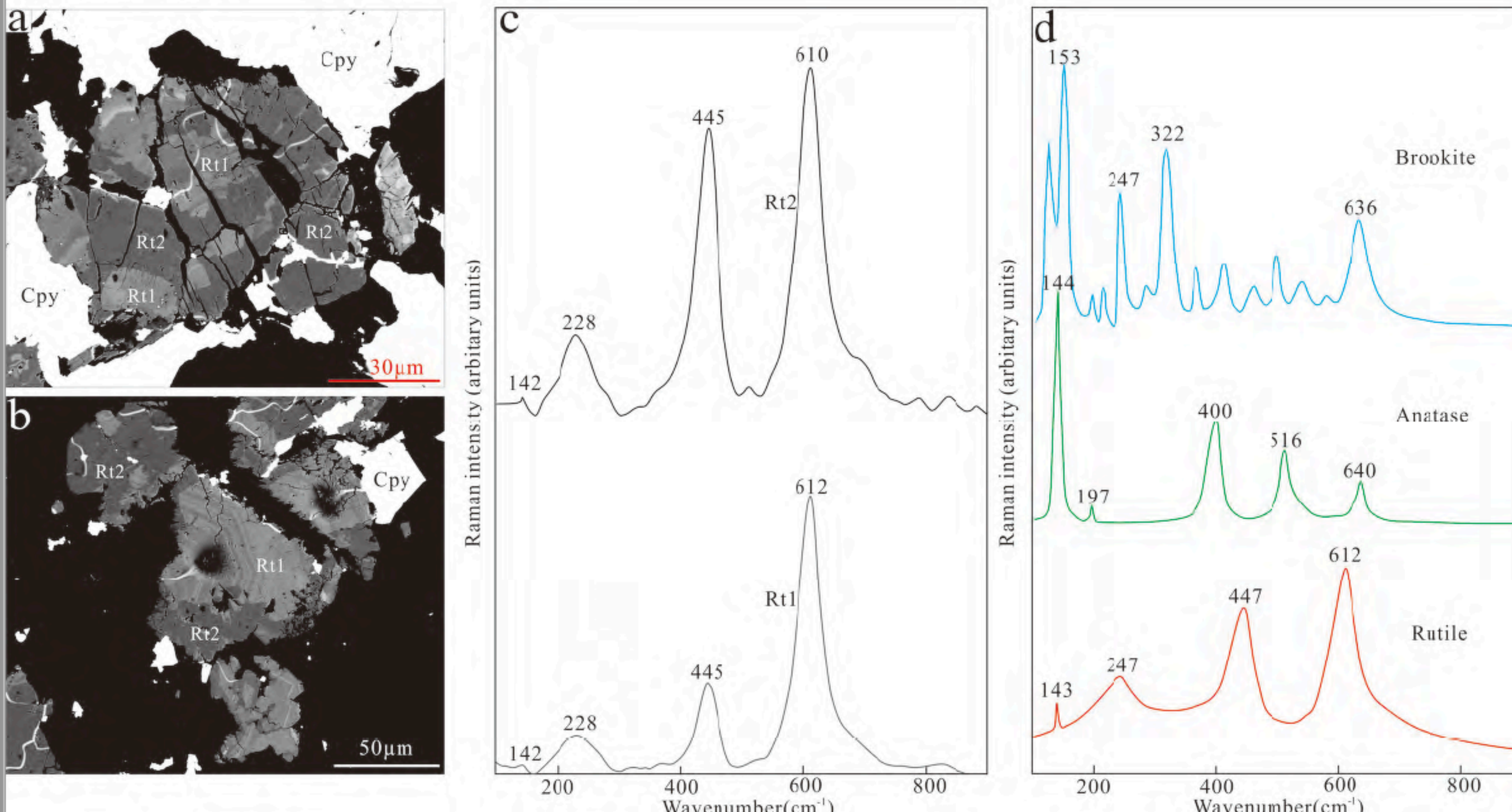
a
Cpy
Rt1
Rt2
Rt2
Cpy
Rt1
30μm
b
Rt2
Cpy
Rt1
Rt2
50μm
c
610
445
Rt2
228
142
612
Rt1
445
228
142
Raman intensity (arbitary units)
200
400
600
800
Wavenumber(cm⁻¹)
d
153
322
Brookite
247
636
144
400
Anatase
516
197
640
612
447
Rutile
247
143
Raman intensity (arbitary units)
200
400
600
800
Wavenumber(cm⁻¹)

Figure 11

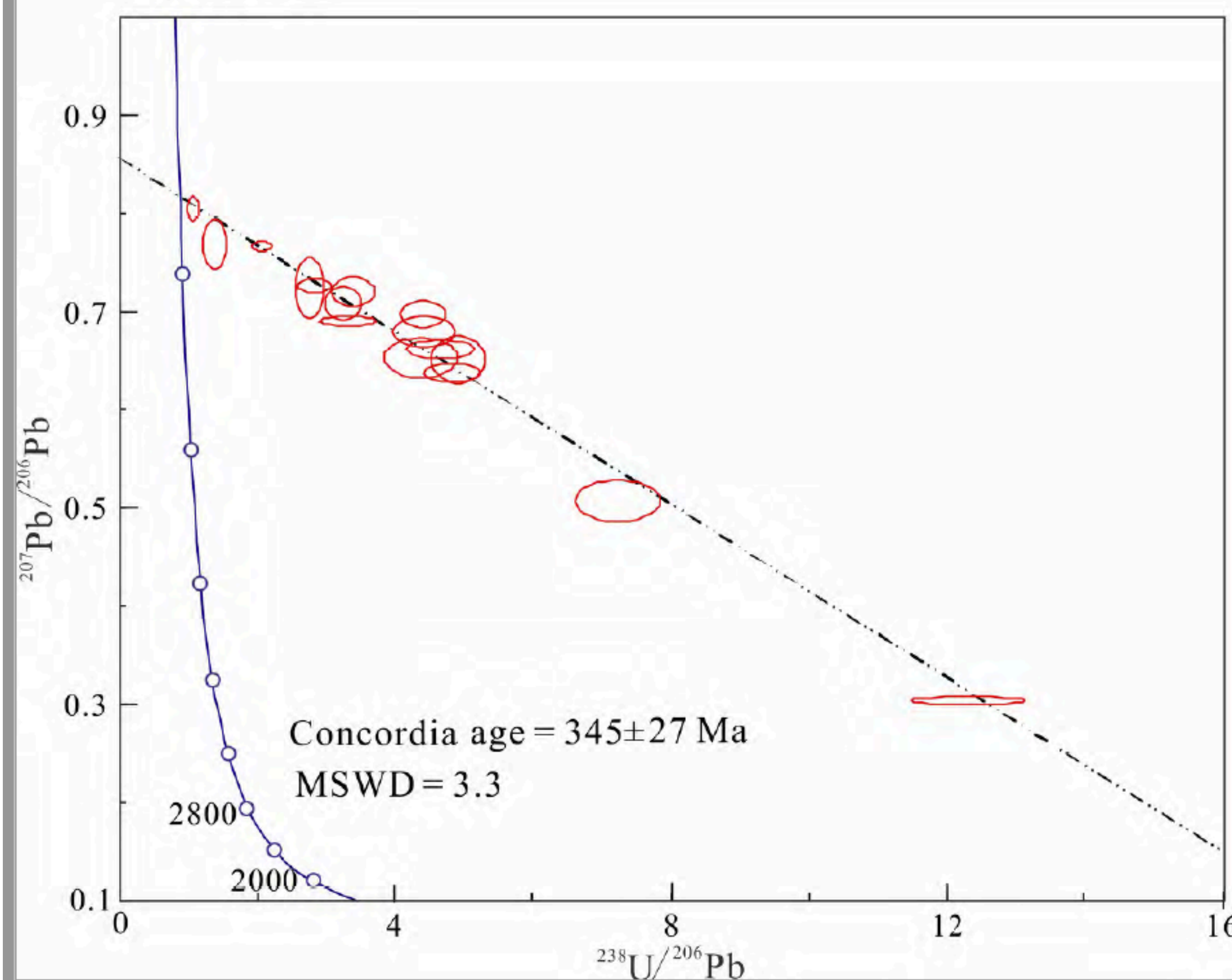

0.9
0.7
0.5
0.3
0.1
0
4
8
12
16
$^{207}Pb/^{206}Pb$
$^{238}U/^{206}Pb$
2800
2000
Concordia age = 345±27 Ma
MSWD = 3.3

Figure 12

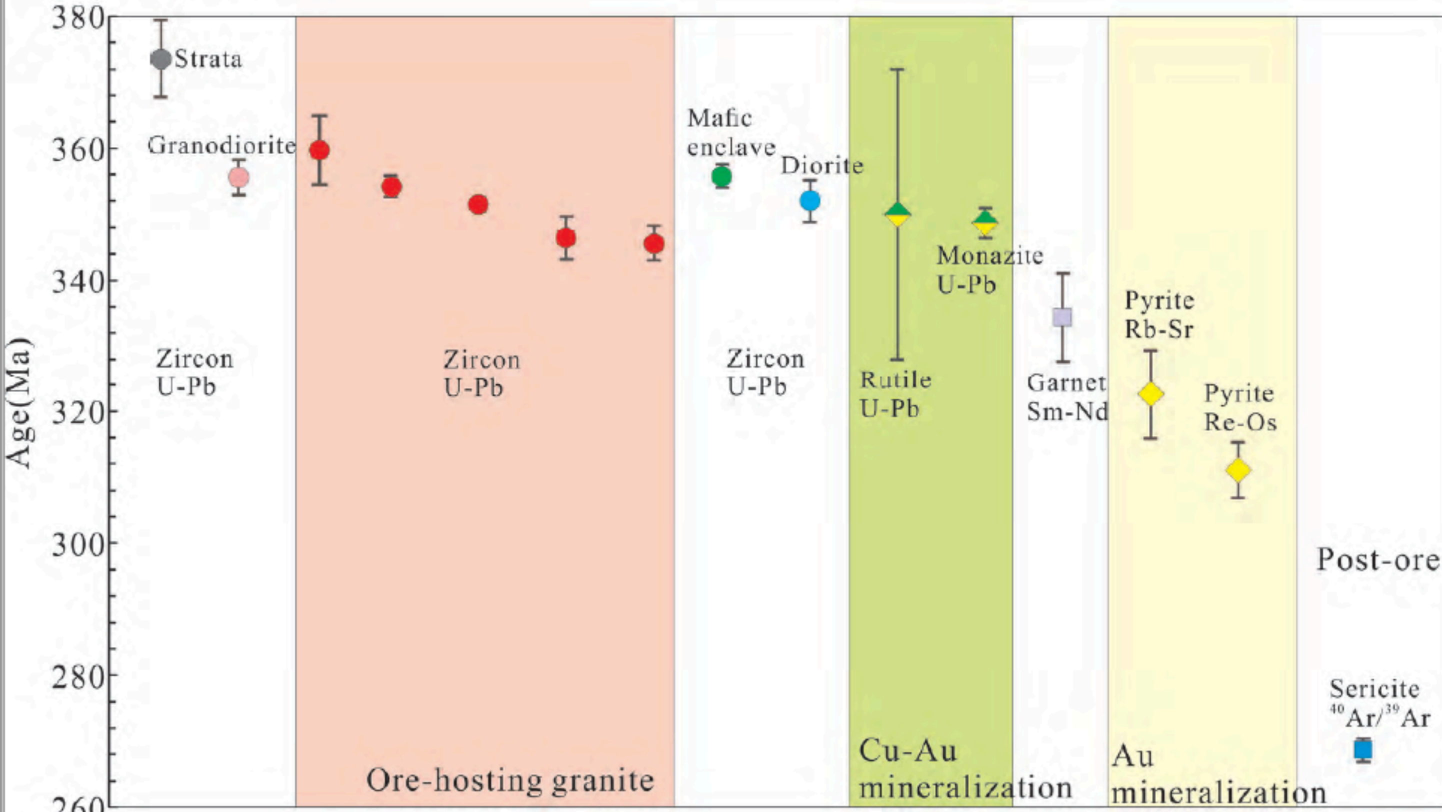

380
360
340
320
300
280
260
Age(Ma)
Strata
Granodiorite
Zircon
U-Pb
Ore-hosting granite
Zircon
U-Pb
Mafic
enclave
Diorite
Zircon
U-Pb
Rutile
U-Pb
Monazite
U-Pb
Cu-Au
mineralization
Garnet
Sm-Nd
Pyrite
Rb-Sr
Pyrite
Re-Os
Au
mineralization
Post-ore
Sericite
$^{40}Ar/^{39}Ar$

Table 1. Zircon SIMS U–Pb isotopic results for the Katbasu granite and mafic enclave

Sample@spot n	Elemental contents									
	U (ppm)	Th (ppm)	Th/U	$^{207}Pb/^{206}Pb$	1SE (%)	$^{207}Pb/^{235}U$	1SE (%)	$^{206}Pb/^{238}U$	1SE (%)	ρ†
Ore-hosted granite										
KT17-187-01	615	512	0.83	0.05362	0.70	0.41821	1.67	0.05657	1.51	0.91
KT17-187-02	1246	837	0.67	0.05426	0.52	0.42071	1.60	0.05624	1.52	0.95
KT17-187-03	738	484	0.66	0.05351	0.60	0.41537	1.63	0.05630	1.52	0.93
KT17-187-04	726	624	0.86	0.05331	0.69	0.41422	1.67	0.05635	1.53	0.91
KT17-187-05	221	164	0.74	0.05364	0.99	0.41439	1.80	0.05603	1.50	0.83
KT17-187-06	579	372	0.64	0.05339	1.16	0.41866	1.91	0.05687	1.51	0.79
KT17-187-07	720	791	1.10	0.05416	0.67	0.41288	1.69	0.05529	1.55	0.92
KT17-187-08	718	567	0.79	0.05327	0.63	0.41750	1.63	0.05684	1.50	0.92
KT17-187-09	701	397	0.57	0.05325	0.51	0.41616	1.59	0.05668	1.51	0.95
KT17-187-10	1300	1181	0.91	0.05411	0.39	0.42059	1.55	0.05637	1.51	0.97
Mafic enclave										
KT17-197-1	1307	1206	0.92	0.05359	0.51	0.41449	1.59	0.05609	1.51	0.95
KT17-197-2	1773	3187	1.80	0.05372	0.37	0.42418	1.55	0.05727	1.50	0.97
KT17-197-3	1235	2078	1.68	0.05396	0.60	0.42855	1.62	0.05760	1.51	0.93
KT17-197-4	2373	4583	1.93	0.05412	0.62	0.42951	1.62	0.05755	1.50	0.92
KT17-197-5	1656	3068	1.85	0.05385	1.82	0.42926	2.35	0.05781	1.50	0.64
KT17-197-6	2841	9160	3.22	0.05347	0.43	0.42658	1.59	0.05786	1.53	0.96
KT17-197-7	770	964	1.25	0.05347	1.15	0.40331	1.89	0.05470	1.50	0.79
KT17-197-8	764	827	1.08	0.05421	0.98	0.40970	1.81	0.05482	1.52	0.84

†ρ denotes error correlation between $^{207}Pb/^{235}U$ and $^{206}Pb/^{238}U$.

§Discordance is defined here as percent deviation of $t_{206/238}$ relative to $t_{207/206}$.

:.

$t_{207/206}$ (Ma)	1SE	$t_{207/235}$ (Ma)	1SE	$t_{206/238}$ (Ma)	1SE	cordance[§] (%)
355.1	15.8	354.8	5.0	354.7	5.2	-0.1
381.8	11.7	356.6	4.8	352.7	5.2	-7.8
350.3	13.5	352.7	4.9	353.1	5.2	0.8
342.1	15.6	351.9	5.0	353.4	5.2	3.4
356.0	22.2	352.0	5.4	351.4	5.1	-1.3
345.5	26.0	355.1	5.7	356.6	5.2	3.3
377.6	15.0	350.9	5.0	346.9	5.2	-8.4
340.4	14.2	354.3	4.9	356.4	5.2	4.8
339.6	11.4	353.3	4.8	355.4	5.2	4.8
375.8	8.7	356.5	4.7	353.5	5.2	-6.1
354.0	11.5	352.1	4.7	351.8	5.2	-0.6
359.3	8.4	359.0	4.7	359.0	5.2	-0.1
369.5	13.4	362.1	5.0	361.0	5.3	-2.4
376.2	14.0	362.8	5.0	360.7	5.3	-4.2
364.9	40.4	362.7	7.2	362.3	5.3	-0.7
348.9	9.8	360.7	4.8	362.6	5.4	4.0
348.9	25.7	344.0	5.5	343.3	5.0	-1.7
379.7	21.8	348.7	5.4	344.0	5.1	-9.7

Table 2. Results of LA-MC-ICP MS zircon U-Pb dating of diorite in the Katbasu Au-Cu deposit.

Spot	Sample number	Th	U	Th/U	$^{207}Pb^*/^{206}Pb^*$		$^{207}Pb^*/^{235}U$		$^{206}Pb^*/^{238}U$		$^{207}Pb/^{206}Pb$ (Ma)		$^{207}Pb/^{235}U$ (Ma)		$^{206}Pb/^{238}U$ (Ma)	
		($\times10^{-6}$)			Ratio	1σ	Ratio	1σ	Ratio	1σ	Age	1σ	Age	1σ	Age	1σ
1	KT17-9-01	361	499	0.72	0.0579	0.0020	0.4636	0.0158	0.0577	0.0007	527.8	77.8	386.8	11.0	361.9	4.5
2	KT17-9-02	128	214	0.60	0.0571	0.0031	0.4728	0.0223	0.0604	0.0010	494.5	118.5	393.1	15.4	378.2	5.8
3	KT17-9-03	263	476	0.55	0.0548	0.0018	0.4392	0.0144	0.0579	0.0006	405.6	75.9	369.7	10.1	362.9	3.8
4	KT17-9-04	224	531	0.42	0.0600	0.0018	0.4951	0.0138	0.0598	0.0006	605.6	97.2	408.4	9.4	374.5	3.9
5	KT17-9-05	197	342	0.58	0.0572	0.0020	0.4766	0.0170	0.0602	0.0007	498.2	77.8	395.7	11.7	377.0	4.2
6	KT17-9-06	682	1015	0.67	0.0554	0.0014	0.4536	0.0111	0.0591	0.0005	427.8	55.6	379.8	7.8	370.1	3.2
7	KT17-9-07	279	426	0.66	0.0582	0.0019	0.5174	0.0167	0.0642	0.0008	600.0	70.4	423.4	11.2	401.2	4.7
8	KT17-9-08	378	1334	0.28	0.0590	0.0013	0.4964	0.0116	0.0608	0.0008	564.9	48.1	409.3	7.9	380.2	4.6
9	KT17-9-09	151	299	0.50	0.0555	0.0019	0.4536	0.0147	0.0591	0.0006	435.2	69.4	379.8	10.3	370.3	3.7
10	KT17-9-10	125	2731	0.05	0.0531	0.0012	0.4600	0.0113	0.0625	0.0008	331.5	53.7	384.2	7.9	391.1	4.6
11	KT17-9-11	243	398	0.61	0.0548	0.0016	0.4574	0.0136	0.0605	0.0007	466.7	66.7	382.5	9.4	378.4	4.4
12	KT17-9-12	1421	1310	1.08	0.0565	0.0014	0.4555	0.0110	0.0583	0.0006	472.3	53.7	381.2	7.6	365.1	3.7
13	KT17-9-13	473	553	0.86	0.0585	0.0023	0.4749	0.0157	0.0583	0.0006	550.0	85.2	394.5	10.8	365.1	3.7
14	KT17-9-14	1345	1935	0.70	0.0522	0.0012	0.4365	0.0106	0.0604	0.0007	300.1	55.6	367.8	7.5	378.1	4.1
15	KT17-9-15	5377	5521	0.97	0.0531	0.0011	0.4163	0.0083	0.0565	0.0005	331.5	44.4	353.4	6.0	354.3	3.1
16	KT17-9-16	384	464	0.83	0.0599	0.0029	0.4585	0.0165	0.0557	0.0005	611.1	100.9	383.2	11.5	349.4	3.2
17	KT17-9-17	389	596	0.65	0.0547	0.0017	0.4253	0.0123	0.0564	0.0006	398.2	75.0	359.8	8.7	353.6	3.4
18	KT17-9-18	393	555	0.71	0.0495	0.0033	0.3764	0.0247	0.0559	0.0006	172.3	157.4	324.4	18.2	350.6	3.6

Table 3. Results of LA-MC-ICP MS U-Pb dating of hydrothermal monazites in the Katbasu Au-Cu deposit.

Spot	Sample number	Pb ($\times10^{-6}$)	Th ($\times10^{-6}$)	U ($\times10^{-6}$)	Th/U	$^{207}Pb/^{206}Pb$		$^{208}Pb/^{232}Th$		$^{206}Pb^{*}/^{238}U$		$^{207}Pb/^{206}Pb$ (Ma)		$^{208}Pb/^{232}Th$ (Ma)		$^{206}Pb/^{238}U$ (Ma)	
						Ratio	1σ	Ratio	1σ	Ratio	1σ	Age	1σ	Age	1σ	Age	1σ
1	KT17-41-1	42	1086	489	2.2	0.0545	0.0038	0.0155	0.0003	0.0566	0.0010	390.8	152.8	311.0	6.0	355.2	5.9
2	KT17-41-2	56	715	910	0.8	0.0529	0.0029	0.0164	0.0005	0.0550	0.0008	324.1	124.1	329.3	10.4	345.3	5.1
3	KT17-41-3	57	1091	789	1.4	0.0532	0.0029	0.0156	0.0003	0.0567	0.0007	344.5	122.2	313.3	5.6	355.4	4.1
4	KT17-41-4	49	1382	539	2.6	0.0602	0.0038	0.0160	0.0003	0.0548	0.0010	613.0	132.4	321.0	5.9	344.0	6.0
5	KT17-41-5	57	1726	625	2.8	0.0501	0.0029	0.0152	0.0002	0.0552	0.0009	198.2	137.0	305.2	4.6	346.6	5.3
6	KT17-41-6	83	855	1339	0.6	0.0537	0.0022	0.0165	0.0003	0.0550	0.0006	366.7	92.6	330.2	6.9	345.2	3.5
7	KT17-41-7	65	2314	598	3.9	0.0522	0.0035	0.0153	0.0002	0.0554	0.0008	294.5	153.7	307.5	4.2	347.8	5.0
8	KT17-41-8	56	2127	471	4.5	0.0555	0.0041	0.0164	0.0003	0.0570	0.0009	435.2	164.8	328.2	5.7	357.1	5.5
9	KT17-41-9	66	1622	816	2.0	0.0529	0.0027	0.0152	0.0002	0.0552	0.0008	324.1	112.0	305.5	4.5	346.2	4.6
10	KT17-41-10	45	930	601	1.5	0.0529	0.0031	0.0160	0.0004	0.0554	0.0008	324.1	131.5	320.2	7.1	347.4	4.9
11	KT17-41-11	61	520	1033	0.5	0.0506	0.0024	0.0158	0.0005	0.0546	0.0007	233.4	109.2	316.6	9.2	343.0	4.3
12	KT17-41-12	71	494	1229	0.4	0.0493	0.0021	0.0151	0.0004	0.0551	0.0007	166.8	100.0	303.0	8.6	345.7	4.1
13	KT17-41-13	86	624	1494	0.4	0.0535	0.0021	0.0161	0.0004	0.0544	0.0006	350.1	88.9	322.2	8.1	341.8	3.7
14	KT17-41-14	50	1156	643	1.8	0.0504	0.0029	0.0170	0.0003	0.0568	0.0008	213.0	133.3	340.0	6.7	356.4	4.8
15	KT17-41-15	35	1090	379	2.9	0.0560	0.0039	0.0178	0.0004	0.0558	0.0011	453.8	155.5	355.7	8.5	350.0	6.7
16	KT17-41-16	43	1589	414	3.8	0.0562	0.0048	0.0164	0.0003	0.0564	0.0012	461.2	189.6	328.1	6.2	353.9	7.4
17	KT17-41-17	53	821	792	1.0	0.0589	0.0029	0.0173	0.0005	0.0560	0.0007	561.1	105.5	345.7	9.1	351.3	4.2
18	KT17-41-18	55	1098	762	1.4	0.0575	0.0029	0.0169	0.0003	0.0549	0.0008	509.3	109.2	339.1	6.8	344.8	5.0
19	KT17-41-19	83	780	1425	0.5	0.0509	0.0020	0.0166	0.0004	0.0542	0.0006	239.0	88.9	333.1	8.3	340.0	3.7
20	KT17-41-20	53	1199	705	1.7	0.0525	0.0026	0.0170	0.0003	0.0565	0.0007	305.6	114.8	340.6	6.5	354.5	4.3
21	KT17-41-21	67	2440	672	3.6	0.0506	0.0029	0.0161	0.0002	0.0566	0.0009	233.4	133.3	322.5	4.2	354.9	5.4
22	KT17-41-22	30	659	410	1.6	0.0528	0.0040	0.0167	0.0004	0.0570	0.0009	320.4	141.7	334.7	7.7	357.3	5.4

23	KT17-41-23	52	2790	308	9.1	0.0554	0.0044	0.0173	0.0003	0.0567	0.0011	431.5	177.8	347.6	6.0	355.8	6.7
24	KT17-41-24	68	741	1151	0.6	0.0565	0.0026	0.0160	0.0004	0.0561	0.0008	472.3	100.0	321.0	8.2	352.0	4.8
25	KT17-41-25	66	2687	582	4.6	0.0532	0.0030	0.0165	0.0002	0.0571	0.0007	338.9	127.8	331.3	4.4	357.9	4.6
26	KT17-41-26	74	758	1310	0.6	0.0528	0.0024	0.0162	0.0004	0.0542	0.0006	316.7	105.5	325.6	7.8	340.5	3.9
27	KT17-41-27	66	1116	1012	1.1	0.0523	0.0026	0.0158	0.0004	0.0561	0.0008	298.2	108.3	316.4	7.0	351.8	4.7

Table 4. Results of SIMS U-Pb dating of W-rich rutile in the Katbasu Au-Cu deposit.

Sample	U (ppm)	Th (ppm)	Th/U	$^{238}U/^{206}Pb^{\#}$	±1σ (%)	$^{207}Pb/^{206}Pb^{\#}$	±1σ (%)	$f^{206\dagger}$	$t_{206/238}^{*}$ (Ma)	±1σ (%)
KT17-40-1	172	118	0.68	12.3224	2.74	0.3036	0.59	40.5	346.4	10.5
KT17-40-2	47	80	1.71	7.2299	3.51	0.5068	1.68	70.6	364.5	21.8
KT17-40-3	80	122	1.52	4.8328	3.44	0.6369	0.57	81.7	330.2	17.1
KT17-40-4	6	6	0.98	4.9332	3.20	0.6502	1.55	81.7	302.2	25.7
KT17-40-5	15	34	2.25	4.3820	4.89	0.6521	1.31	88.2	336.1	31.5
KT17-40-6	81	43	0.53	4.6627	4.34	0.6611	0.66	80.2	300.8	20.3
KT17-40-7	20	83	4.13	4.4222	4.21	0.6795	0.97	98.8	284.1	23.6
KT17-40-8	34	51	1.53	3.3209	5.11	0.6905	0.29	90.9	350.4	22.4
KT17-40-9	14	49	3.49	3.2505	3.30	0.7081	1.01	96.6	315.2	27.7
KT17-40-10	6	23	3.66	3.3929	3.82	0.7197	0.87	98.5	275.0	25.1
KT17-40-11	31	134	4.33	2.7836	2.98	0.7241	1.75	96.9	321.8	45.5
KT17-40-12	17	69	3.97	2.8436	3.66	0.7262	0.37	98.3	309.3	18.7
KT17-40-13	39	164	4.24	2.0561	2.83	0.7664	0.27	99.6	271.1	15.6
KT17-40-14	8	24	2.90	1.3853	4.86	0.7683	1.32	96.9	388.8	76.1
KT17-40-15	11	94	8.33	1.0668	3.61	0.8045	0.65	106.6	235.4	47.6
KT17-40-16	24	64	2.70	4.3994	3.06	0.6974	0.86	100.5	253.3	18.5

$^{\#}$ The ratios are common Pb uncorrected, used for Tera–Wasserburg plot.

$^{\dagger}f^{206}$ is the percentage of common ^{206}Pb in total ^{206}Pb, calculated by ^{207}Pb-based.

$^{*}t_{206/238}$ is $^{206}Pb–^{238}U$ age calculated by ^{207}Pb-based common-lead correction.